Neurobiology of Disease

Deletion of Transferrin Receptor 1 in Parvalbumin Interneurons Induces a Hereditary Spastic Paraplegia-Like Phenotype

Wenchao Xiong,[1*] Liqiang Jin,[1*] Yulu Zhao,[1] Yu Wu,[2] Jinghua Dong,[1] Zhixin Guo,[1] Minzhen Zhu,[1] Yongfeng Dai,[1] Yida Pan,[1] and Xinhong Zhu[1,2,3]
[1]School of Basic Medical Sciences, Southern Medical University, Guangzhou 510515, China, [2]School of Psychology, Shenzhen University, Shenzhen 518060, China, and [3]Research Center for Brain Health, Pazhou Lab, Guangzhou 510330, China

Hereditary spastic paraplegia (HSP) is a severe neurodegenerative movement disorder, the underlying pathophysiology of which remains poorly understood. Mounting evidence has suggested that iron homeostasis dysregulation can lead to motor function impairment. However, whether deficits in iron homeostasis are involved in the pathophysiology of HSP remains unknown. To address this knowledge gap, we focused on parvalbumin-positive (PV^+) interneurons, a large category of inhibitory neurons in the central nervous system, which play a critical role in motor regulation. The PV^+ interneuron-specific deletion of the gene encoding transferrin receptor 1 (TFR1), a key component of the neuronal iron uptake machinery, induced severe progressive motor deficits in both male and female mice. In addition, we observed skeletal muscle atrophy, axon degeneration in the spinal cord dorsal column, and alterations in the expression of HSP-related proteins in male mice with *Tfr1* deletion in the PV^+ interneurons. These phenotypes were highly consistent with the core clinical features of HSP cases. Furthermore, the effects on motor function induced by *Tfr1* ablation in PV^+ interneurons were mostly concentrated in the dorsal spinal cord; however, iron repletion partly rescued the motor defects and axon loss seen in both sexes of conditional *Tfr1* mutant mice. Our study describes a new mouse model for mechanistic and therapeutic studies relating to HSP and provides novel insights into iron metabolism in spinal cord PV^+ interneurons and its role in the regulation of motor functions.

Key words: **axon degeneration; hereditary spastic paraplegia; motor; parvalbumin; spinal cord; transferrin receptor 1**

Significance Statement

Iron is crucial for neuronal functioning. Mounting evidence suggests that iron homeostasis dysregulation can induce motor function deficits. Transferrin receptor 1 (TFR1) is thought to be the key component in neuronal iron uptake. We found that deletion of *Tfr1* in parvalbumin-positive (PV^+) interneurons in mice induced severe progressive motor deficits, skeletal muscle atrophy, axon degeneration in the spinal cord dorsal column, and alterations in the expression of hereditary spastic paraplegia (HSP)-related proteins. These phenotypes were highly consistent with the core clinical features of HSP cases and partly rescued by iron repletion. This study describes a new mouse model for the study of HSP and provides novel insights into iron metabolism in spinal cord PV^+ interneurons.

Introduction

Hereditary spastic paraplegia (HSP) is a rare upper motor neurodegenerative disease characterized by progressive lower-limb spasticity (Shribman et al., 2019). HSP can be triggered at any age and affects significantly more males than females (Schüle et al., 2016). HSP is also associated with complications such as ataxia, seizures, mental retardation, and sensory loss. The most prominent neuropathological sign is axon degeneration in corticospinal tracts and the fasciculus gracilis (Fink, 2013). To date, 79 "spastic gait" loci have been identified (Shribman et al., 2019). Despite advances in the understanding of HSP genetics, the underlying pathogenesis of the disease remains largely unclear and no treatments for HSP are currently available.

Received Dec. 12, 2022; revised June 1, 2023; accepted June 5, 2023.

Author contributions: X.Z. designed research; W.X., L.J., Y.Z., J.D., Z.G., M.Z., Y.D., and Y.P. performed research; W.X., L.J., and Y.W. analyzed data; W.X. wrote the first draft of the paper; X.Z. wrote the paper.

This work was supported by National Natural Science Foundation of China Grants 81930034 (to X.Z.) and 32000682 (to W.X.), the STI 2030–Major Project Grant 2022ZD0211700 (to X.Z.), and the China Postdoctoral Science Foundation Grant 2020M672705 (to W.X.). We thank Dr. Lijun Zhou, Yingtao Jie, and Yuan Tang (Sun Yat-Sen University) for technical supports in the spinal cord-related experiments; Dr. Xinsheng Lai (Nanchang University) for providing polyclonal antibodies against Syn/NF; and Dr. Mingqiang Li (Pazhou Lab) for radiological imaging. We also thank Shuji Li, Ying Li, Yingying Fang, Ting Guo, Xiaowen Li (Southern Medical University), Shengquan Zheng, Xi Wu, and Hao Liu (Pazhou Lab) for their technical supports.

[*] W.X. and L.J. contributed equally to this work.

The authors declare no competing financial interests.

Correspondence should be addressed to Xinhong Zhu at zhuxh527@126.com.

https://doi.org/10.1523/JNEUROSCI.2277-22.2023

Iron is crucial for neuronal functioning through its role in processes such as oxygen transportation, mitochondrial respiration, myelin production, axon maturation, and neurotransmitter metabolism (Ward et al., 2014; Möller et al., 2019). Iron homeostasis dysregulation has been implicated in various movement disorders, including Parkinson's disease, multiple sclerosis, Friedreich's ataxia, Huntington's disease, restless leg syndrome and attention-deficit hyperactivity disorder (Rouault, 2013; Ward et al., 2014; Tseng et al., 2018). Iron deficiency during development can alter the expression of motor disorder-associated genes (Clardy et al., 2006). Infants with iron deficiency show poor motor function (de Andraca et al., 1997; Shafir et al., 2008, 2009). In animals, iron deficiency in dopaminergic neurons can lead to neurodegeneration and motor deficits (Matak et al., 2016) and abnormal axonal iron transport between brain regions induces hyperactivity (Z. Wang et al., 2019). These observations indicate that iron homeostasis is important for motor function; however, whether iron homeostasis disruption is involved in the pathophysiology of HSP remains unknown.

Parvalbumin-positive (PV$^+$) interneurons, comprising a large category of inhibitory neurons in the central nervous system, play a critical role in motor regulation. Striatal PV$^+$ interneurons facilitate movement by refining the activation of medium spiny neuron networks (Gritton et al., 2019). PV$^+$ interneuron activity regulates motor output (Estebanez et al., 2017; Pamukcu et al., 2020), and has been implicated in several motor-related neurodegenerative disorders, including amyotrophic lateral sclerosis, Huntington's disease, Parkinson's disease, Alzheimer's disease (Verret et al., 2012; Friedman et al., 2020; Woodin et al., 2020; Paldino et al., 2022). Moreover, early-life iron deficiency results in reductions in mRNA and protein levels of PV in the brain (Callahan et al., 2013; Bastian et al., 2014), indicating that iron plays a key role in maintaining normal functions of PV$^+$ interneuron. However, whether iron of PV$^+$ interneurons contributes to motor function is unknown.

Transferrin receptor 1 (TFR1), the key component of the neuronal iron uptake machinery, is abundantly expressed in neurons and is required for the endocytosis of the diferric transferrin/TFR1 complex (Rouault, 2013; Muckenthaler et al., 2017). TFR1 also has a role in intracellular signaling. Studies showed that TFR1 stearoylation can affect the mitochondrial fission/fusion process, which is involved in the maintenance of axonal homeostasis (Senyilmaz et al., 2015; Misgeld and Schwarz, 2017). Studies have demonstrated the importance of TFR1 in erythroid cells (Levy et al., 1999), cardiomyocytes (Xu et al., 2015), muscle cells (Barrientos et al., 2015; Wu et al., 2021), the intestinal epithelium (A.C. Chen et al., 2015), T cells (Z.Z. Wang et al., 2018), neural progenitor cells (Liu et al., 2016), Schwann cells (Santiago González et al., 2019), Purkinje cells (Zhou et al., 2017) and dopaminergic neurons (Matak et al., 2016).

Here, we investigated the role of iron in PV$^+$ interneurons by crossing PV-Cre mice with *Tfr1*$^{fl/fl}$ mice to generate PV-Cre; *Tfr1*$^{fl/fl}$ (*Tfr1*-cKO) mice, and found that *Tfr1*-cKO mice exhibited severe progressive motor impairment, skeletal muscle atrophy, and corticospinal axon degeneration, phenotypes that are highly consistent with the clinical features of patients with HSP. Importantly, iron dextran administration partly rescued these motor deficits. Our results indicate that *Tfr1*-cKO mice may serve as a genetic model for the study of HSP and that iron deficiency in PV$^+$ interneurons of dorsal spinal cord contributes to neurodegeneration and motor deficits.

Materials and Methods

Animals

Transgenic mice PV-Cre (catalog #017320, RRID: IMSR_JAX:017320), Cre-dependent ROSA26 tdTomato reporter (Ai9, catalog #007909, RRID: IMSR_JAX:007909) and *Tfr1*$^{fl/fl}$ (catalog #028177, RRID: IMSR_JAX:028177) mouse lines were purchased from Jackson Laboratory, and bred in the exhaust ventilated closed-system cage (EVC) at 24 ± 1°C. C57BL/6J male mice (aged 8–10 weeks) were obtained from the Southern Medical University Animal Center (No: SCXK-2021-0041, Guangzhou, China). *Tfr1*-cKO mice were bred by crossing PV-Cre; *Tfr1*$^{fl/wt}$ with *Tfr1*$^{fl/fl}$ mice. PV-tdTomato mice were bred by crossing PV-Cre and Ai9 mice. All mice were fed *ad libitum* and were provided with unrestricted, clean drinking water under standard laboratory conditions in a 12/12 h light/dark cycle (lights on 8 A.M. to 8 P.M.). All mouse lines were generated on the C57BL/6J background. All animal experiments were conducted in strict accordance with the Regulations for the Administration of Affairs Concerning Experimental Animals, and were approved by the Animal Ethics Committee of Southern Medical University. Behavioral tests were performed during the same circadian period (1–6 P.M.) by experimenters blinded to the experimental design.

Virus construction and packaging

The virus was purchased from Shanghai OBiO Technology Co, Ltd. The shRNA sequence targeting *Tfr1* (GenBank accession: NM_011638) was 5′-CCGACAATAACATGAAGGCTA-3′. The viral titer for *Tfr1*-shRNA administration was 8.15×10^{12} viral genomes (vg)/ml.

Stereotactic injection

For brain injection, six- to eight-week-old PV-Cre male mice were anesthetized with isoflurane (3% induction, 1.5% maintenance) and then fixed in a stereotaxic apparatus (RWD, 68861N), covering their eyes with eye ointment to prevent corneal drying. The mice were injected with 200 nl of the *Tfr1*-shRNA virus into brain regions through a 5-µl Hamilton syringe connected to a glass electrode. The injection sites included the primary motor cortex (MC; AP = +1.58 mm, ML = ±1.80 mm, DV = −1.0 mm), the reticular thalamic nucleus (RT; AP = −0.58 mm, ML = ±1.30 mm, DV = −2.0 mm) and substantia nigra (SN; AP = −3.16 mm, ML = ±1.50 mm, DV = −4.5 mm). 5 min after virus injection, the injection needle was slowly retracted from the injection site. After surgery, the scalp was sutured, and the mice were put on a heating pad until reviving.

For spinal cord injection, eight-week-old PV-tdTomato male mice (for the ventral spinal cord) or PV-Cre mice (for the dorsal spinal cord) were anesthetized with isoflurane (3% induction, 1.5% maintenance). Following anesthesia induction, the most caudal rib was localized and traced to Vertebra L1. Dorsal laminectomies were performed at the L1 vertebral level. After affixing the spine, the *Tfr1*-shRNA virus was injected with 250 nl into the lumbar spinal cord through a 5-µl Hamilton syringe connected to a glass electrode, whereas the control group was injected with the scrambled shRNA [negative control (NC)-shRNA] virus. According to the dorsal spinal vein, the stereotactic coordinates included the dorsal spinal cord (ML = ±0.25 mm, DV = −0.3 mm) and the ventral horn of the spinal cord (ML = ±0.3 mm, DV = −0.75 mm).

For skeletal muscle injection, we injected 360 µl *Tfr1*-shRNA or NC-shRNA virus into the skeletal muscles of eight-week-old PV-Cre mice, with 6 sites per leg (30 µl/site), and performed the behavioral tests one month later. The virus was diluted to 1.0×10^{10} v.g./ml in 0.1 M PBS.

Osmotic minipump implantation

C57BL/6J mice were anesthetized, and a micro-osmotic pump (Alzet, Model 1004) was implanted into the right side of the lateral ventricle using stereotaxic coordinates (AP = −0.58 mm, ML = +1.1 mm, DV = −2 mm). The connected osmotic pump was placed beneath the dorsal subcutaneous tissue. The mice were constantly infused with 18 mM deferiprone (DFP; Sigma-Aldrich catalog #379409-5G) or artificial CSF (ACSF) into the lateral ventricle at a speed of 0.11 µl/h for 28 d. The scalp wound was then stitched with 3M Vetbond Tissue Adhesive (3M catalog #1469SB). After surgery, the mice were placed back into their home cages for a 14-d recovery period.

Immunostaining

Mice were deeply anesthetized with 1% pentobarbital and transcardially perfused with PBS buffer (pH 7) followed by 4% paraformaldehyde (PFA). Brains, spinal cord, and muscle were postfixed in PFA overnight and immersed in 30% sucrose dissolved in PBS.

For brain immunofluorescence staining, brain sections were cut into 40-µm-thick sections, and the spinal cords were cut into 25-µm-thick cross-sections using a freezing microtome (Leica, CM1950), and subsequently washed in 0.1 M PBS three times for 10 min. The sections were then incubated and permeabilized in blocking buffer (10% BSA with 0.3% Triton X-100 in 0.1 M PBS) for 2 h at room temperature. Subsequently, the sections were incubated in primary antibodies at 4°C overnight. All sections were then washed in PBS three times for 10 min and incubated with a secondary antibody for 2 h at room temperature. Following secondary antibody incubation, the sections were washed three times for 15 min in PBS and mounted with 4',6-diamidino-2-phenylindole (DAPI; Vector Labs). Fluorescence images were acquired under an A1R confocal microscope (Nikon Instruments).

PV$^+$ neurons were quantified in brain regions using the software ImageJ (National Institutes of Health). The samples were prepared from eight slices across the brain regions of each mouse. The 25×25 µm region of interest was outlined in the cerebellum around torpedoes and calculated as previously described (Ljungberg et al., 2016). PV$^+$ and choline O-acetyltransferase-positive (ChAT$^+$) neurons were counted in eight sections of the lumbar spinal cord (L1–L5) from *Tfr1*-cKO mice and wild-type (WT) littermates. ChAT$^+$ neurons were calculated in the ventral horn of the spinal cord using the software ImageJ (National Institutes of Health). PV$^+$ neurons were counted in different parts of the spinal cord, including the spinal cord dorsal column. ChAT, PV and SMI-312 fluorescent intensity was quantified using NIS Elements version 4.5 (Nikon Instruments). Regular and irregular axons were quantified in dorsal column as previously reported (Qiang et al., 2019). Stereological counting and section quantification were double blinded.

For immunofluorescence staining, cultured dorsal root ganglia (DRG) neurons growing on coverslips were fixed in 4% PFA at room temperature for 20 min. The following steps were performed in accordance with brain section staining. Imaris 8.3 (Bitplane) was used for neuron reconstruction and sholl analysis, including the number of intersections and length of the longest neurite. For muscle spindle analysis, fresh muscles were serially sectioned into 20-µm slices and one in every 10 sections was transferred onto 2% gelatinized glass slides. Sections were blocked with goat serum, 0.3% Triton X-100 in PBS for 1 h at room temperature, and then incubated with primary antibody overnight at 4°C. After washing three times with 0.1 M PBS, the sections were incubated with secondary antibody for 2 h at room temperature, washed, and mounted with DAPI. Fluorescence images were acquired under a VS200 slide scanner (Olympus). Individual muscle spindles were identified through sequential serial sections and the total number of muscle spindles was counted. For neuromuscular junction staining, muscle tissues were cut into 100-µm sections and incubated with 100 mM glycine in PBS for 1 h at room temperature and then blocked in goat serum, 0.3% Triton X-100 in PBS for 1 h. The slices were stained in primary antibody overnight at 4°C, followed by washout and secondary antibody incubation for 2 h at room temperature. The sections were mounted with DAPI and images were acquired under an A1R confocal microscope (Nikon Instruments).

The antibodies used were mouse anti-PV (1:1000; Swant catalog #235, RRID: AB_10000343), rabbit anti-PV (1:1000; Swant catalog #PV27, RRID: AB_2631173), rabbit anti-TFR1 (1:400, Novus catalog #NB100-92243, RRID: AB_1216384), rabbit anti-TH (1:1000, Abcam catalog #ab112, RRID: AB_297840), goat anti-ChAT (1:500, Novus catalog #NBP1-30 052, RRID: AB_2079586), mouse anti-SMI-312 (1:500, Biolegend catalog #837904, RRID: AB_2566782), rabbit anti-Tuj1 (1:800, Abcam catalog #ab18207, RRID: AB_444319), mouse anti-NF (1:500, Cell Signaling Technology catalog #2835, RRID: AB_490808), rabbit anti-Syn (1:500, Cell Signaling Technology catalog #36406, RRID: AB_2799098), Alexa Fluor 594 goat anti-rabbit IgG (1:500, Thermo Fisher Scientific catalog #A-11037, RRID: AB_2534095), Alexa Fluor 594 goat anti-mouse IgG (1:500, Thermo Fisher Scientific catalog #A-11032, RRID: AB_141672), Alexa Fluor 488 goat anti-rabbit IgG (1:500, Thermo Fisher Scientific catalog #A-11034, RRID: AB_2576217), Alexa Fluor 488 goat anti-mouse IgG (1:500, Thermo Fisher Scientific catalog #A-11001, RRID: AB_2534069), Alexa Fluor 647 donkey anti-goat IgG (1:500, Thermo Fisher Scientific catalog #A32849, RRID: AB_2762840), and Alexa Fluor 594-conjugated α-bungarotoxin (α-BTX; 1:2000, Thermo Fisher Scientific catalog #B35450).

Hematoxylin/eosin (H&E) staining

The muscle tissues were embedded in paraffin and cut into 4-µm sections, and the sections were then used for H&E staining according to the manufacturer's instructions. The muscle cross-sectional areas and the cell diameter were recorded. For the brain and spinal cord, 30-µm-thick sections were cut on a freezing microtome (Leica, CM1950).

Western blotting

Tissues were homogenized, centrifuged, and quantified using a BCA Protein Assay kit (Thermo Fisher Scientific catalog #23225). Once the protein concentration was quantified, total protein was loaded on SDS-PAGE gels (10%). The separated proteins were then transferred to polyvinylidene fluoride membranes. After blocking with skimmed milk, the membranes were incubated with one of the following primary antibodies: rabbit anti-TFR1 (1:1000; Abcam catalog #ab84036, RRID: AB_10673794), goat anti-ChAT (1:100, Novus catalog #NBP1-30052, RRID: AB_2079586), rabbit anti-PV (1:1000; Swant catalog #PV27, RRID: AB_2631173), or mouse anti-GAPDH (1:1000; Hangzhou Goodhere Biotechnology catalog #AB-M-M001). Protein bands were visualized using Western Lighting ECL (PerkinElmer) after incubation in secondary antibodies, peroxidase-conjugated AffiniPure goat anti-rabbit IgG (H+L), donkey anti-goat IgG (H+L) and donkey anti-mouse IgG (H+L; 1:5000, ZSGB-Bio). Proteins levels were normalized to GAPDH. All results were analyzed with AlphaEase-FC (Alpha Innotech Corp.).

Quantitative real-time PCR (q-PCR)

Total RNA was extracted from the dorsal spinal cord of *Tfr1*-cKO mice and their control littermates using RNAiso Plus (Takara) according to the manufacturer's protocol and quantified using the NanoDrop 2000 (Thermo Scientific). The PrimeScript RT Reagent kit (Takara) was used for cDNA synthesis. Quantitative real-time PCR was performed in an ABI 7500 Real-Time PCR System with SYBR premix EX Taq (Takara). Relative mRNA levels were normalized to S18 rRNA levels and calculated using the $\Delta\Delta$Ct method. The sequences of the primers used for qPCR were as follows (F, forward; R, reverse): *Fth* (F: 5′-CCATCAACCGCCAGATCAAC-3′, R: 5′-GCCACATCATCTCGGTCAAA-3′); *Ftl* (F: 5′-GGGCCTCCTACACCTACCTC-3′, R: 5′-CTCCTGGGTTTTACCCCATT-3′); *Slc11a2* (F: 5′-CCTGGACTGTGGACGCT-3′, R: 5′-GGTGTTCAGAAGATAGAGT-3′); *Irp1* (F: 5′-TTAGGGTTTGATGTGGTGGG-3′, R: 5′-TGTGTTAGGATGGACTCGGC-3′), *Irp2* (F: 5′-TGACCTACAGAAAGCAGGAAAG-3′, R: 5′-GCTCTCCAGAATCACACGAT-3′); *Tfr1* (F: 5′-TCAAGCCAGATCAGCATTCTC-3′, R: 5′-AGCCAGTTTCATCTCCACATG-3′); *Rps18* (F: 5′-AGTTCCAGCACATTTTGCGAG-3′, R: 5′-TCATCCTCCGTGAGTTCTCCA-3′).

Iron detection

For the detection of serum iron, blood was collected through retro-orbital bleeding. After allowing to stand at room temperature for 2 h, the blood was centrifuged for 10 min at 4500 rpm, and the supernatant was collected and stored at 4°C until further processing. For the detection of spinal cord tissue iron, mice were perfused with physiological saline, and the tissue was dissected. After weighing, concentrated, nitric acid (Fisher Chemical catalog #A509-P212) was added to the tissue according to the recorded weight (1:40), after which the samples were heated at 75°C for 2 h on a constant temperature metal bath heater. Finally, serum and spinal cord iron concentrations were determined using graphite furnace

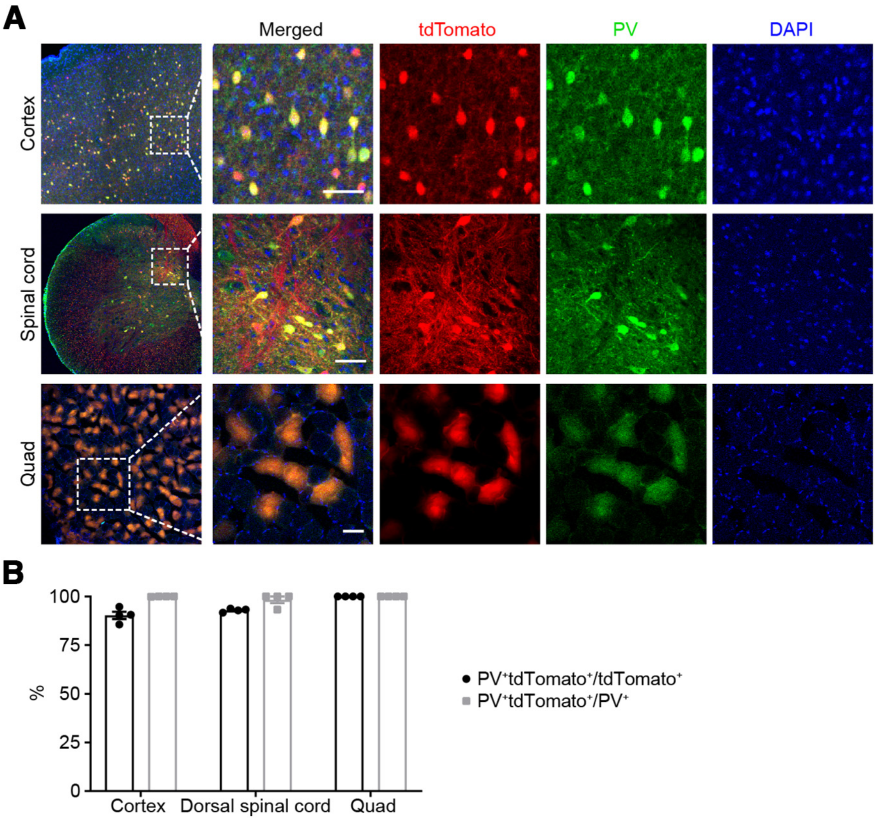

Figure 1. tdTomato-positive cells of PV-tdTomato mice reacted to PV antibody. ***A***, Immunostaining for PV (green) in the cortex, spinal cord, and quadriceps femoris muscles (Quad) of PV-tdTomato mice. ***B***, Quantification of tdTomato and PV expression. $n = 4$ mice per group. Scale bar: 50 μm. Data are expressed as means ± SEM.

atomic absorption spectrometry (PinAAcle 900Z, PerkinElmer) according to the manufacturer's instructions.

Radiologic imaging

Mice were anesthetized with pentobarbital sodium (intraperitoneal), placed in a stable anatomic position to restrict movement, and then subjected to x-ray microcomputed tomography (60 kV, 500 μA). Three-dimensional image reconstruction was performed using RadiAnt DICOM Viewer.

Pole test

The pole test was conducted as previously reported (Nuber et al., 2018). Briefly, the mice were placed at the top of a vertical pole (50 cm in height and 1 cm in diameter) and tested for their ability to descend the pole (snout first) by recording the time from initiating the head down movement to all four paws reaching the platform. The average times to "climb down" were calculated from five consecutive trials, and the maximum time was set to 60 s.

Beam test

Mice were trained to walk across a horizontal beam (100 cm in length, 4 cm in width, and 20 cm in height) to their home cages on the first day. On the next day, the mice were recorded beam-walking using a video camera. Each mouse was tested three times separately. The video recordings were quantified into frames to calculate the foot-to-base angle (FBA) at toe-off positions of the hind paws. In total, 12 foot-to-base angles were assessed per mouse for analysis.

Rotarod

Rotarod is an experiment for evaluating the balance and motor performance on a ROTA-ROD apparatus (Panlab Harvard). On the first day, the mice were placed on the rod of the equipment rotating at 4 rpm and allowed to adapt to the running state for ∼5 min. The next day, the mice were put onto the rotarod at the same speed (4 rpm) for habitation until accelerating the rotarod from 4 to 40 rpm in 5 min. The time until falling off the beam was recorded. Each mouse had a 5-min interval between trials and were tested for three trials per day for two consecutive days.

Gait analysis

Gait analysis was performed as previously described (Wertman et al., 2019), using the following tunnel measurements: 35 cm in length, 7 cm in width, 8 cm in height. A smooth paper was placed inside the tunnel, and the goal chamber was placed at the end of the tunnel. The mice were grasped gently, and the paws were painted, using one color for hind-limbs, and another for forelimbs. The mice were allowed to walk through the tunnel to the goal chamber and should take enough steps (more than four) to collect the data. The footprints created by the same foot were counted to calculate the stride width and length. Five steps were counted to calculate the average distance.

Clasping

For clasping evaluation, the mice were held by their tails, and their behaviors were analyzed for 10 s. If dystonic movements occurred on one side of hindlimb, they scored 1 point, and on both sides, 2 points. The mice scored three points when displaying a combination of hindlimb and trunk clasping (Nuber et al., 2018).

Y-maze

Y-maze was performed as described previously (W.J. Chen et al., 2020). Briefly, mice were placed in the center area of a frosted plastic Y-maze (30 cm in length,10 cm in width, and 20 cm in height) and allowed to explore freely for 5 min. Simultaneously, the succession of arm entries was recorded using an overhead camera, and the data were analyzed to calculate the alteration percentage. After each trial, the Y-maze was cleaned with 70% ethanol.

Acoustic startle response

Prepulse inhibition was performed as previously described (De Pace et al., 2018). Briefly, acoustic startle response was measured on an SR-Lab system (San Diego Instruments) for ∼40 min. Each mouse was placed into a startle chamber and habituated for 5 min to a 65-dB white noise background. After the habituation, the mice were exposed to a total of 120 trials, ranging from 70 to 120 dB, with 10 trials per intensity within a random time interval (5–25 s). The startle response was recorded in 100 ms, measuring the peak of the startle response. The % prepulse inhibition was calculated as follows: 100 – [(startle response on acoustic prepulse plus startle stimulus trials/startle response-alone trials) × 100].

Neuronal culture

As previously described (Lin and Chen, 2018), DRG neurons were collected from postnatal day (P)30 to P40 mice. Coated the glass slides with poly-lysine overnight and then washed with sterilized water. The mice were euthanized with an overdose of pentobarbital sodium; then, their skin was removed, and the spinal column was collected from the forelimbs to the femur. DRGs were separated to ice-cold culture medium under a stereo microscope. Subsequently, DRGs were incubated in preheated 2 ml 0.05% trypsin and collagenase (1:1) for 40 min at 37°C before stopping the digestion. After centrifuging at 900 rpm for 2 min, we removed the supernatant solution, adding 2 ml serum-free medium to the cell pellets and mixing by pipetting up-down gently, using a 70-μm cell strainer (Falcon) to filter the cells. Lastly, the cells were centrifuged at

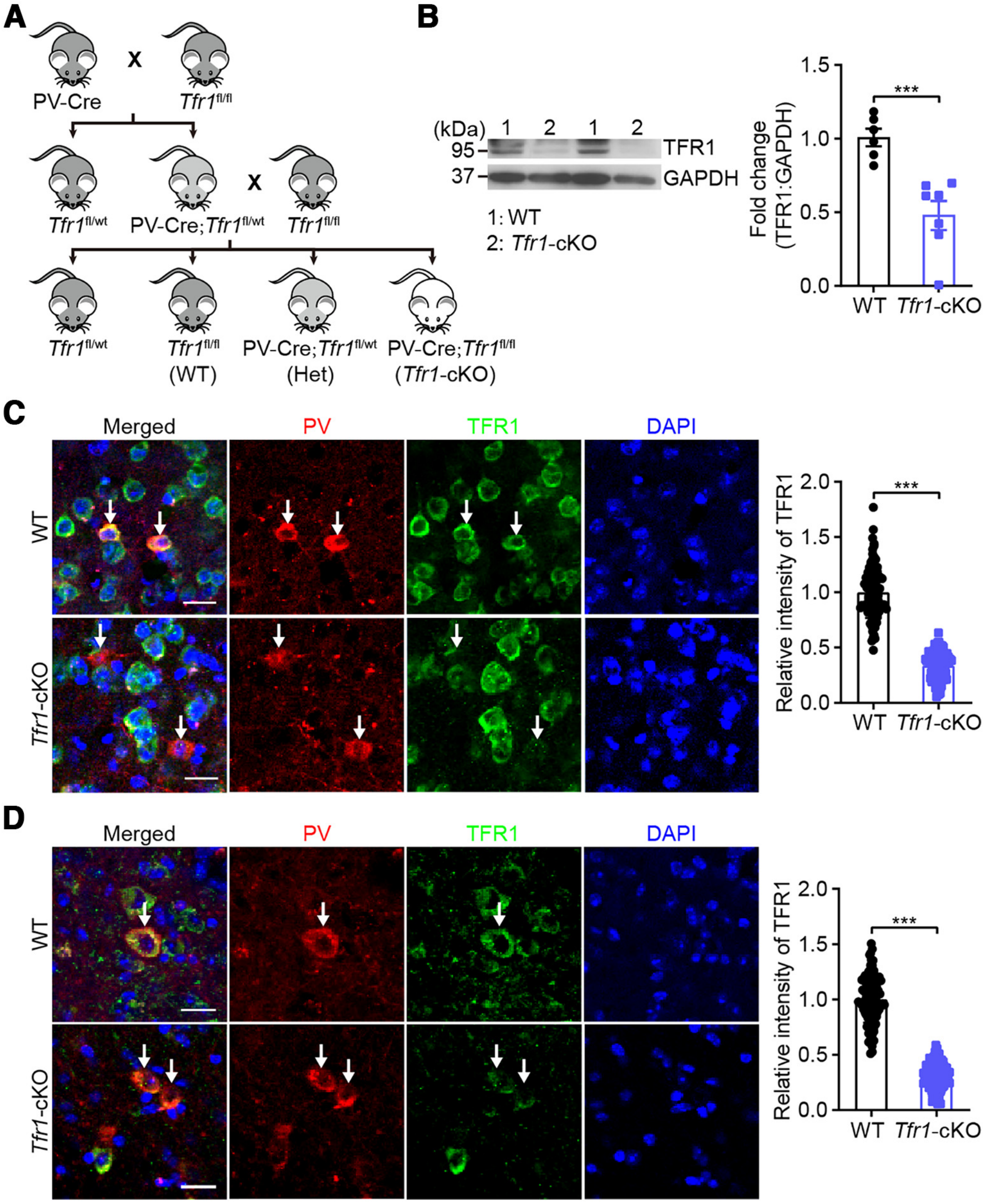

Figure 2. Generation of *Tfr1*-cKO mice. ***A***, Breeding strategy for *Tfr1*-cKO mice. ***B***, Western blot analysis of TFR1 in gastrocnemius muscle of *Tfr1*-cKO and WT male mice. $n = 6–7$ mice per group. ***C***, PV (red) and TFR1 (green) immunofluorescence staining in the cortex of *Tfr1*-cKO and WT male mice. $n = 100$ PV^+ neurons from four mice per group. ***D***, Immunostaining for PV (red) and TFR1 (green) in the spinal cord. $n = 100$ PV^+ neurons from four mice per group. Scale bar: 50 μm. Data are expressed as means ± SEM; $^{***}p < 0.001$.

900 rpm for 5 min and seeded after re-suspension in culture medium. The culture medium for DRG neurons was Neurobasal Medium-A (Invitrogen catalog #10888-022) 500 ml + B27 (Invitrogen catalog #17504-044) 10 ml + Glutamax 100× (Invitrogen catalog #35050-061) 5 ml + Cytarabine (final concentration: 5 μM). For pharmacology experiments, 36 h after plating onto glass slides, cells were treated with 75 μM $Fe(NH_4)_2(SO_4)_2$ (Sigma-Aldrich catalog #203505) for 24 h.

Cortical neurons were prepared from embryonic day 17 mouse embryos using Neurobasal Medium (Invitrogen catalog #21103-049) 500 ml + B27 10 ml + Glutamax 100 × 5 ml. Subsequently, 7 d after plating onto a Petri dish, cells were treated with 75 μM $Fe(NH_4)_2(SO_4)_2$ for 24 h and collected for PRM.

Iron dextran treatment

Mice were intraperitoneally injected with 5 mg iron dextran (Sigma-Aldrich catalog #D8517-25ML) or PBS at P10 and P20 and the behavioral tests were conducted at P40 and P60.

Protein extraction and trypsin digestion

Proteomics analysis was performed by four-dimensional label-free quantification mass spectrometry. Mice were deeply anesthetized and transcardially perfused with PBS buffer (pH 7) and the spinal cord was removed from the lumbar enlargement on ice. The tissues were refrigerated at −80°C and shipped on dry ice.

For protein extraction and digestion, samples were homogenized and dissolved in lysis buffer consisting of 8 M urea (Sigma-Aldrich) and 1% Protease Inhibitor Cocktail (Merck Millipore). The lysates were sonicated three times on ice using a high-intensity ultrasonic processor (Scientz) and then centrifuged at 12,000 × *g* at 4°C for 10 min. The sample supernatant was collected into a new tube and quantified with the Microplate BCA Protein Assay kit (Thermo Scientific). According to the BCA results, the tissues were adjusted to consistency. Subsequently, the extracted proteins were precipitated with 20% trichloroacetic acid for 2 h at 4°C. After centrifugation at 4500 × *g* for 5 min, the tissues were discarded, and the supernatant was washed in ice-cold acetone for two to three times. The protein was re-dissolved in sample buffer (8 M urea,

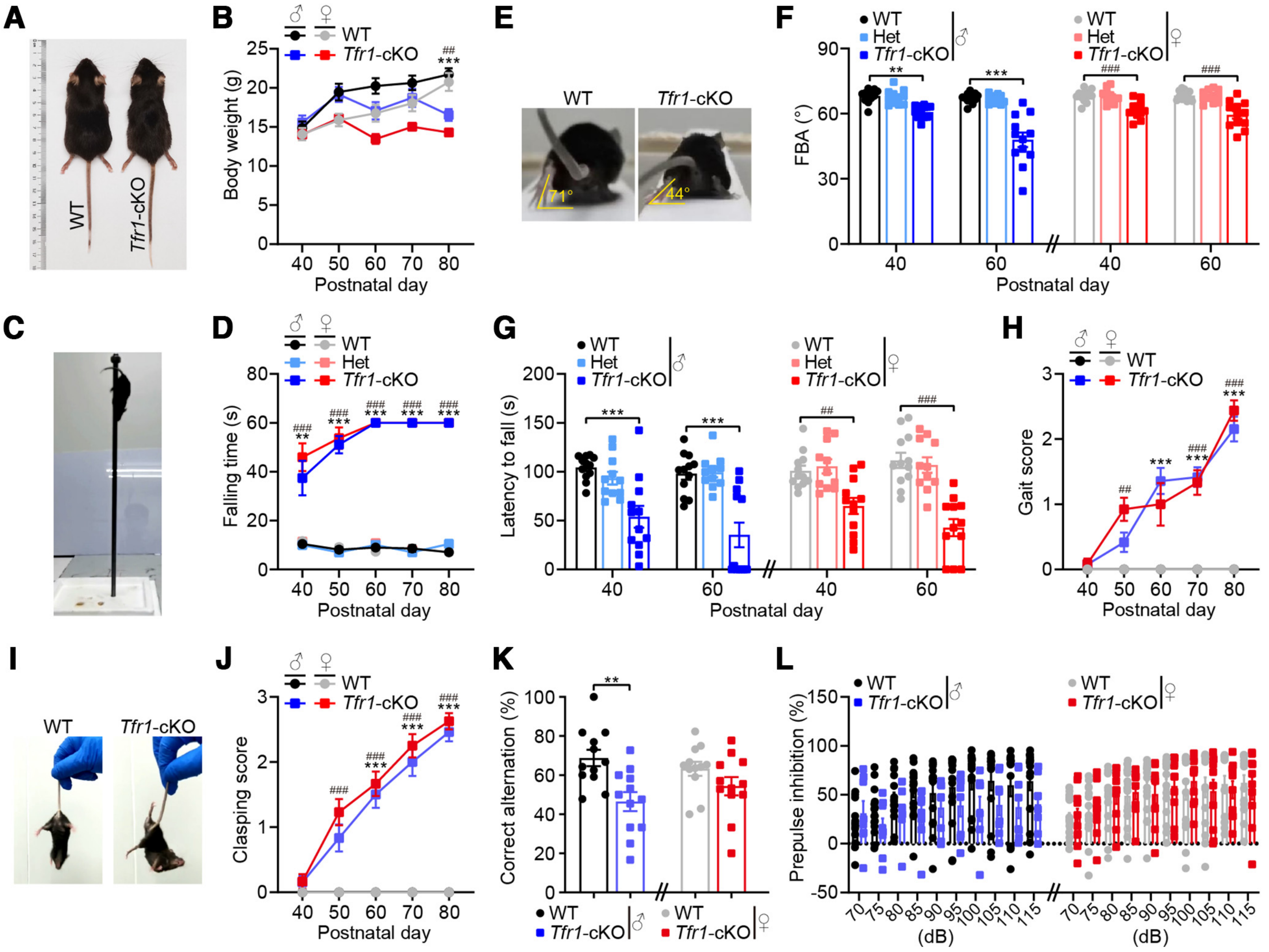

Figure 3. *Tfr1*-cKO mice showed severe, progressive motor abnormalities. ***A***, Representative image of WT and *Tfr1*-cKO male mice at P80. ***B***, The body weight of male and female mice. $n = 8–12$ mice per group. ***C***, Representative, single movie frame of a WT female mouse descending the pole in the pole test. ***D***, Age-dependent measurement of latency to descend in the pole test for *Tfr1*-cKO mice, heterozygous (Het) mice, and WT control littermates. $n = 11–15$ mice per group. ***E***, Representative single movie frames of 80-d-old WT and *Tfr1*-cKO male mice walking on a beam following the removal of the toe of the hindlimb. The FBA is indicated by yellow lines. ***F***, The FBA decreased over time in *Tfr1*-cKO mice compared with that in their WT littermates. $n = 11–12$ mice per group. ***G***, The latency to fall off an accelerating rotarod decreased over time in *Tfr1*-cKO mice when compared with that in WT mice. $n = 11–12$ mice per group. ***H***, Gait score in *Tfr1*-cKO versus WT mice from P40 to P80. $n = 12–15$ mice per group. ***I***, Sixty-day-old mice lifted by the tail showed normal spreading of the lower limbs (WT mice) or limb-spasm behavior (*Tfr1*-cKO mice). ***J***, Limb clasping in *Tfr1*-cKO versus WT mice from P40 to P80. $n = 12–16$ mice per group. ***K***, Percentage of correct alternation for *Tfr1*-cKO and WT mice at P40 in the Y-maze test. $n = 12$ mice per group. ***L***, Acoustic startle response of 40-d-old mice subjected to increased noise levels in decibels (dB). $n = 8–15$ mice per group. ♂: males, ♀: females. Data are expressed as means ± SEM; $^{**}p < 0.01$, $^{***}p < 0.001$, male *Tfr1*-cKO mice versus WT mice; $^{\#\#}p < 0.01$, $^{\#\#\#}p < 0.001$, female *Tfr1*-cKO mice versus WT mice.

100 mM triethylammonium bicarbonate, pH 8.0). The tissues were then diluted by adding 200 mM triethylammonium bicarbonate buffer (Sigma-Aldrich) and sonicated via ultrasound. Then, trypsin was reduced with 5 mM dithiothreitol (Sigma-Aldrich) for 30 min at 56°C. The protein solution was alkylated with 11 mM iodoacetamide (Sigma-Aldrich) for 15 min at room temperature in darkness.

Liquid chromatography-mass spectrometry analysis and proteomics analysis

The samples were analyzed on an EASY-nLC 1200 ultrahigh performance liquid chromatography system coupled to an Orbitrap Exploris 480 Mass spectrometer. The tryptic peptides were dissolved in solvent A. The gradient setting consisted of an increase from 6 to 23% solvent B within 70 min, 23–32% within 14 min, and increased to 80% within 5 min and then left standing for 5 min. Solvent A consisted of 0.1% formic acid and 2% acetonitrile in water, while solvent B consisted of 0.1% formic acid in 90% acetonitrile. Full scans were performed at a resolution of 60,000, with a scan range of 400–1200 m/z, and an automatic gain control target of 600,000 charges. The data were analyzed on an Orbitrap Exploris 480 Mass spectrometer.

Secondary mass spectrometry data were searched for using Proteome Discoverer (v2.4.1.15) and Uniprot Mus_musculus_10090_SP_20210721 database concatenated with the reverse decoy database. Trypsin/P was specified as cleavage enzyme allowing up to two missing cleavages. The mass tolerance for fragment ions was set to 0.02 Da. Carbamidomethyl on Cys was specified as a fixed modification, and acetylation on the protein N terminus and oxidation on Met were specified as variable modifications. False discovery rate (FDR) was adjusted to < 1%. In order to eliminate any variations caused by unequal mixing, the resulting data set was auto-bias-corrected. In this correction, most proteins were assumed to have maintained their expression levels. Using this bias correction, systematic errors related to inequalities in the amount of samples taken from each experimental condition were mitigated. All quantification results were then based on the median average protein ratio. Protein identification was supported by all peptide matches with 95% confidence. When p-value < 0.05 and fold change > 1.5, the protein was considered differentially expressed.

Parallel reaction monitoring (PRM)

Peptide extraction and tryptic digestion were performed as described above. A total of 50 proteins selected for PRM validation were based on the results of the proteomic analysis. The tryptic peptides were dissolved in solvent A on an NanoElute UPLC system. The gradient settings consisted of an increase from 6 to 24% solvent B within 18 min, from 24 to 35% within 6 min, an increase up to 80% within 3 min; the samples were then left standing for last 3 min at a constant flow of 450 nl/min. Solvent A consisted of 0.1% formic acid and 2% acetonitrile in water, while solvent B consisted of 0.1% formic acid in 90% acetonitrile. The peptides were subjected to a nano-spray-ionization source followed by tandem mass spectrometry (MS/MS) in timesTOF Pro. The MS/MS mass range scans were performed at 100–1700 m/z. The data were acquired in PRM-parallel accumulation serial fragmentation mode.

The secondary mass spectrometry data were searched for in the MaxQuant (v1.6.15.0) and Uniprot Mus_musculus_10090_SP_20210721 databases concatenated with the reverse decoy database. Trypsin/P was specified as the cleavage enzyme allowing up to two missing cleavages. The minimum peptide length was 7, and the maximum number of modifications was set to 5. The first precursor tolerance database search was performed at 20 ppm, while the main search was performed at 4.5 ppm. The second precursor tolerance database search was performed at 20 ppm, selecting Cysteine Carbamidomethylation (C) as a fixed modification, and methionine oxidation, protein N-terminus acetylation, and deamidation (NQ) as variable modifications and using a FDR threshold of 1%. The data were analyzed using Skyline 21.1 software.

Experimental design and statistical analyses

All the data were analyzed using GraphPad Prism 8 (GraphPad Software) and are presented as means ± SEM. Unpaired Student's *t* tests (two-tailed) or multiple *t* tests were used for comparisons between two groups. One-way ANOVA (when equal variance was assumed) or Dunnett's T3 *post hoc* test (when homogeneity of variance was not assumed) was employed for comparisons among three or more groups. Repeated measures ANOVA followed by a Bonferroni *post hoc* test for multiple comparisons was used to evaluate possible differences between groups if there were no missing values, whereas a mixed-effects model was used if values were missing. Two-way ANOVA followed by a Bonferroni *post hoc* test for multiple comparisons was used to analyze the possible effects of iron dextran treatment. The significance level for all tests was set at $p < 0.05$.

Results

Conditional ablation of *Tfr1* in PV$^+$ interneurons

To investigate the role of iron homeostasis in PV$^+$ interneurons, we employed a PV-driven Cre knock-in mouse line. To validated the Cre expression, we crossed PV-Cre mice with Ai9 mice and slices were co-stained with anti-PV antibodies. We found that nearly all PV$^+$ positive cells were tdTomato$^+$ cells, and >90% of tdTomato$^+$ cells in the cortex, dorsal spinal cord and skeletal muscle were PV$^+$ cells (Fig. 1*A*,*B*). We then generated conditional *Tfr1* knock-out mice (*Tfr1*-cKO) by crossbreeding PV-Cre mice with homozygous *Tfr1* floxed mice (*Tfr1*$^{fl/fl}$), yielding the PV-Cre;*Tfr1*$^{fl/fl}$ line. Because *Tfr1*-cKO adult mice displayed severe motor dysfunction and had difficulties in mating, to produce *Tfr1*-cKO mice, we crossed adult PV-Cre; *Tfr1*$^{fl/wt}$ (Het) mice, which showed normal behaviors, with *Tfr1*$^{fl/fl}$ mice. *Tfr1*$^{fl/fl}$ [wild-type (WT)] littermates of *Tfr1*-cKO mice served as controls (Fig. 2*A*). It has been shown that PV is abundantly expressed in skeletal fast muscles (Heizmann et al., 1982). Here, Western blot analysis indicated that TFR1 protein levels were markedly lower in the skeletal muscle of *Tfr1*-cKO mice than in that of their control littermates (Fig. 2*B*; $t_{(11)} = 4.592$, $p = 0.0008$, unpaired Student's *t* test). Additionally, immunohistochemistry results showed that, compared with control animals, TFR1 fluorescence intensity was significantly decreased in PV$^+$ neurons in both the brain (Fig. 2*C*; $t_{(198)} = 25.32$, $p < 0.0001$, unpaired Student's *t* test) and spinal cord (Fig. 2*D*; $t_{(198)} = 28.68$, $p < 0.0001$, unpaired Student's *t* test) of *Tfr1*-cKO mice. These results demonstrated that *Tfr1* expression in PV$^+$ interneurons was efficiently disrupted in *Tfr1*-cKO mice.

Movie 1. *Tfr1*-cKO mice displayed gait impairment (1 M-male). Left, WT. Right, *Tfr1*-cKO. [View online]

Movie 2. *Tfr1*-cKO mice displayed gait impairment (2 M-male). Left, WT. Right, *Tfr1*-cKO. [View online]

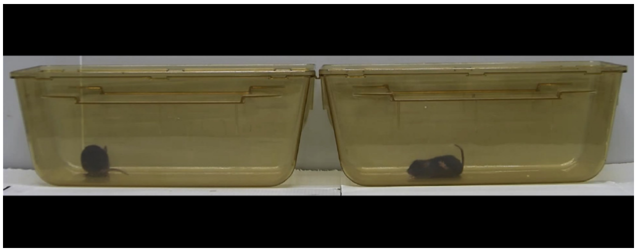

Movie 3. *Tfr1*-cKO mice displayed gait impairment (3 M-male). Left, WT. Right, *Tfr1*-cKO. [View online]

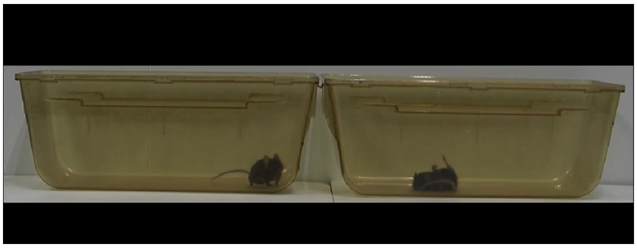

Movie 4. *Tfr1*-cKO mice displayed gait impairment (4 M-male). Left, WT. Right, *Tfr1*-cKO. [View online]

Tfr1-cKO mice displayed severe, progressive motor deficits

We generated a cohort of mice consisting of *Tfr1*-cKO, Het and matched WT animals, and subjected them to behavioral tests on

Movie 5. Pole test (WT: P60-female). [View online]

Movie 6. Pole test (*Tfr1*-cKO: P60-female). [View online]

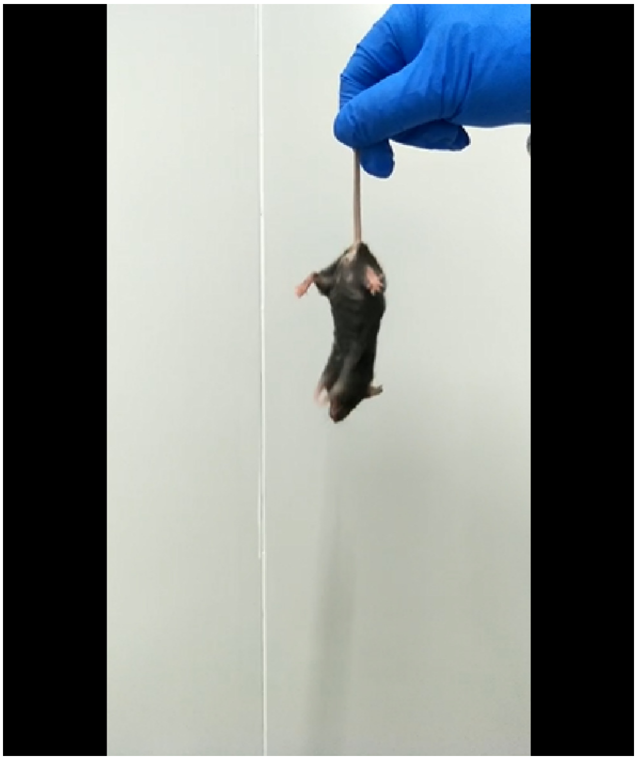

Movie 7. Clasping (WT: P60-female). [View online]

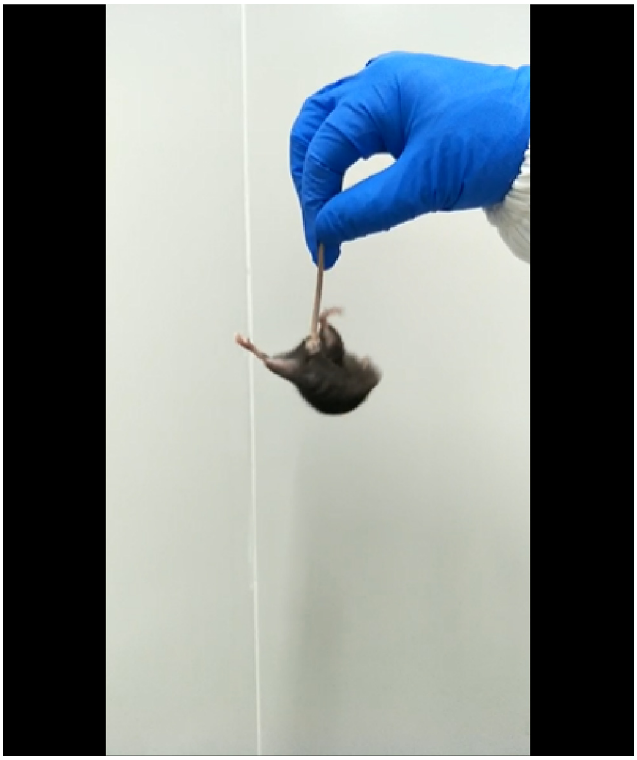

Movie 8. Clasping (*Tfr1*-cKO: P60-female). [View online]

P40, P50, P60, P70, and P80. We found that body size was slightly decreased with increasing age between the two groups (Fig. 3*A*,*B*; Male: group, $F_{(1,18)}$ = 1.874, $p < 0.0001$; interaction, $F_{(4,69)}$ = 23.48, $p < 0.0001$; Female: group, $F_{(1,18)}$ = 5.187, $p = 0.0352$; interaction, $F_{(4,70)}$ = 60.65, $p < 0.0001$, mixed-effects model). Initially, no difference in body weight was observed between *Tfr1*-cKO mice and their WT littermates; however, at P80, *Tfr1*-cKO mice displayed a significant loss of body weight when compared with control animals, possibly because of difficulty in accessing food (Fig. 3*B*). To determine whether

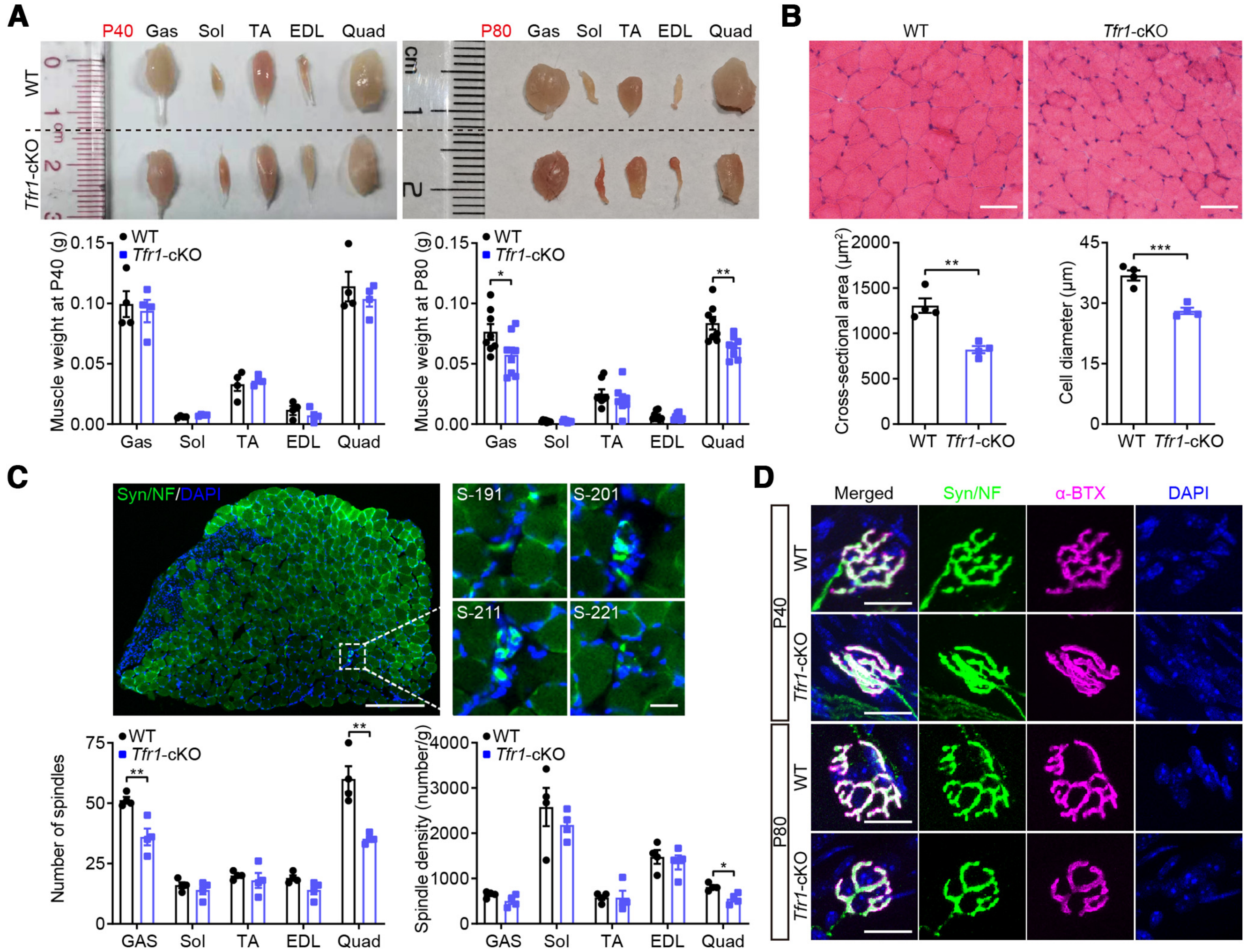

Figure 4. Skeletal muscle atrophy was observed in *Tfr1*-cKO mice. ***A***, Comparison of the morphology and wet weight of skeletal muscle between WT and *Tfr1*-cKO male mice at P40 and P80. Gas: gastrocnemius muscle; Sol: soleus muscle; TA: tibialis anterior muscle; EDL: extensor digitorum longus muscle; Quad: quadriceps femoris muscle. P40: $n = 4$ mice per group; P80: $n = 8$ mice per group. ***B***, H&E staining of transectioned quadriceps muscle fibers showed that the fiber area and the diameter of the cells in the quadricep muscles were smaller in *Tfr1*-cKO male mice than in their WT littermates at P80. $n = 4$ mice per group. ***C***, Top, Serially sectioned soleus muscles were immunostained with Syn/NF (green) to identify muscle spindles. S-191/201/211/221: section 191/201/211/221. Bottom, Total number and density of muscle spindles in *Tfr1*-cKO male mice and their WT littermates at P80. $n = 4$ mice per group. ***D***, An intact neuromuscular junction in the gastrocnemius muscle stained with α-BTX (magenta) and Syn/NF (green). Scale bar: 50 μm (***B***); 200 μm (***C***, top left); 20 μm (***C***, top right, ***D***). Data are expressed as means ± SEM; $^{*}p < 0.05$, $^{**}p < 0.01$, $^{***}p < 0.001$.

movement was impaired in *Tfr1*-cKO mice, we filmed the mice while they moved freely in their cages. Both male and female *Tfr1*-cKO mice exhibited abnormal motor performance, mainly gait disturbances, spasticity in the lower limbs, and difficulty with balance, which worsened with age, almost to paralysis (Movies 1, 2, 3, 4). Next, we analyzed in detail their motor deficits as a function of age and sex using the pole, beam balance, rotarod, clasping, and gait tests. In the pole test, *Tfr1*-cKO mice either immediately fell off the pole or descended it significantly more slowly compared with their control littermates (Fig. 3*C*,*D*; Movies 5, 6; Male: group, $F_{(2,37)} = 601.2$, $p < 0.0001$; interaction, $F_{(8135)} = 7.622$, $p < 0.0001$; Female: group, $F_{(2,38)} = 795.6$, $p < 0.0001$; interaction, $F_{(8,130)} = 4.933$, $p < 0.0001$, mixed-effects model). In the beam test, *Tfr1*-cKO mice displayed gait disturbances at P40, which became severe at P60, as quantified by measurement of the FBA (Fig. 3*E*,*F*; Male: group, $F_{(2,32)} = 44.66$, $p < 0.0001$; interaction, $F_{(2,32)} = 9.707$, $p = 0.0005$; Female: group, $F_{(2,32)} = 22.04$, $p < 0.0001$; interaction, $F_{(2,32)} = 1.457$, $p = 0.2479$, two-way repeated measures ANOVA). In an accelerating rotarod, *Tfr1*-cKO mice exhibited decreased latency to falling off, with several mice even immediately falling off the rotarod at P60 (Fig. 3*G*; Male: group, $F_{(2,32)} = 18.46$, $p < 0.0001$; interaction, $F_{(2,32)} = 2.561$, $p = 0.0930$; Female: group, $F_{(2,32)} = 20.54$, $p < 0.0001$; interaction, $F_{(2,32)} = 5.714$, $p = 0.0076$, two-way repeated measures ANOVA). No differences were detected between Het and WT mice in the three tests (Fig. 3*D*,*F*,*G*). Because the 80-d-old *Tfr1*-cKO mice were unable to perform the beam balance and rotarod tests, we conducted the gait and clasping tests to assess their motor coordination. *Tfr1*-cKO mice showed altered gait (Fig. 3*H*; Male: group, $F_{(1,27)} = 192.4$, $p < 0.0001$; interaction, $F_{(4,96)} = 31.28$, $p < 0.0001$; Female: group, $F_{(1,28)} = 112.1$, $p < 0.0001$; interaction, $F_{(4,90)} = 21.02$, $p < 0.0001$, mixed-effects model) and hind-limb clasping (Fig. 3*I*,*J*; Movies 7, 8; Male: group, $F_{(1,27)} = 264.1$, $p < 0.0001$; interaction, $F_{(4,96)} = 30.36$, $p < 0.0001$; Female: group, $F_{(1,28)} = 296.9$, $p < 0.0001$; interaction, $F_{(4,90)} = 38.84$, $p < 0.0001$, mixed-effects model) scores compared with their WT littermates. To examine the effect of TFR1 ablation in PV^{+} interneurons on cognition, we performed the Y-maze spontaneous

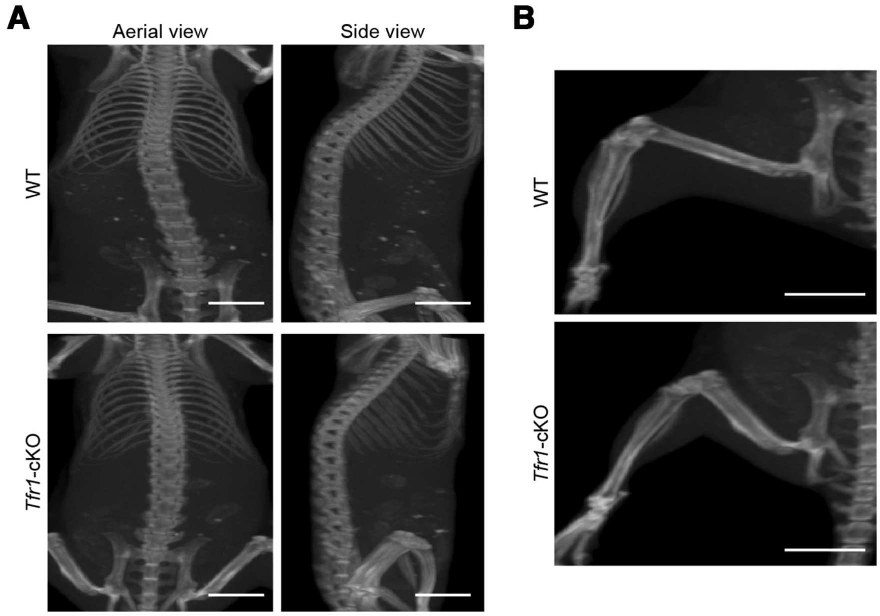

Figure 5. No structural deformity was observed in the spine or hindlimbs of *Tfr1*-cKO mice. ***A***, Bone morphology of the spine in a male *Tfr1*-cKO mouse and a control littermate at P80. ***B***, Radiologic images showing the bone structure of the hindlimb of a male *Tfr1*-cKO mouse and a control littermate at P80. Scale bar: 5 mm.

alternation test. *Tfr1*-cKO mice performed worse than their WT littermates in the Y-maze test, although the difference was significant only in male mice (Fig. 3*K*; Male: $t_{(22)} = 3.435$, $p = 0.0024$; Female: $t_{(22)} = 1.553$, $p = 0.1347$, unpaired Student's *t* test). Given that motor actions and sensory processing are inextricably linked, we examined the response of the mice to loud acoustic stimuli in the acoustic startle response test and found no differences between mice of the two groups (Fig. 3*L*; Male: group, $F_{(1,21)} = 2.436$, $p = 0.1335$; interaction, $F_{(9,189)} = 1.702$, $p = 0.0909$; Female: group, $F_{(1,23)} = 0.000$, $p = 0.9895$; interaction, $F_{(9,207)} = 0.6496$, $p = 0.7536$, two-way repeated measures ANOVA). In addition, in the rotarod test, 7/12 male *Tfr1*-cKO mice at P60 fell straight off the rotarod, compared with only 3/12 females, suggesting that motor impairment was more severe in male *Tfr1*-cKO mice than in their female counterparts. Taken together, these results indicated that *Tfr1* disruption in PV^{+} interneurons in mice leads to distinct lower-limb spasticity and progressive weakness.

Tfr1-cKO mice showed skeletal muscle atrophy

Given that neuromuscular junctions are essential for motor function (Legay and Mei, 2017), we next assessed whether *Tfr1* ablation in PV^{+} interneurons affected skeletal muscles. First, we analyzed muscle morphology in the hindlimbs. No significant difference in weight was found between *Tfr1*-cKO and WT mice at P40; however, at P80, the weights of the gastrocnemius and quadriceps femoris muscles of *Tfr1*-cKO mice were reduced compared with those of the controls (Fig. 4*A*; P40: GAS, $t_{(6)} = 0.4024$, $p = 0.7014$; Sol, $t_{(6)} = 2.186$, $p = 0.0714$; TA, $t_{(6)} = 0.5139$, $p = 0.6257$; EDL, $t_{(6)} = 1.098$, $p = 0.3145$; Quad, $t_{(6)} = 0.7804$, $p = 0.4648$, unpaired Student's *t* test; P80: GAS, $t_{(14)} = 1.768$, $p = 0.0989$; Sol, $t_{(14)} = 0.1201$, $p = 0.9061$; TA, $t_{(14)} = 0.8202$, $p = 0.4258$; EDL, $t_{(14)} = 0.7756$, $p = 0.4509$; Quad, $t_{(14)} = 3.195$, $p = 0.0065$, unpaired Student's *t* test). Moreover, H&E staining showed that the fiber area and the diameter of cells in the quadriceps muscles of *Tfr1*-cKO mice were smaller than those of their WT littermates (Fig. 4*B*; Cross-sectional area: $t_{(6)} = 5.383$, $p = 0.0017$, unpaired Student's *t* test; Cell diameter: $t_{(6)} = 6.074$, $p = 0.0009$, unpaired Student's *t* test). As altered muscle morphology may be associated with spindle or motor neuron degeneration (Yang et al., 2021), we also immunestained skeletal muscles with anti-synaptophysin/neurofilament (Syn/NF) antibodies. Histologic analysis showed that, compared with control animals, *Tfr1*-cKO mice exhibited reduced muscle spindle number in gastrocnemius and quadriceps muscles, and lower spindle density in quadriceps muscles (Fig. 4*C*; Number of spindles: GAS, $t_{(6)} = 4.091$, $p = 0.0064$; Sol, $t_{(6)} = 0.9258$, $p = 0.3902$; TA, $t_{(6)} = 0.6273$, $p = 0.5536$; EDL, $t_{(6)} = 2.402$, $p = 0.0532$; Quad, $t_{(6)} = 4.552$, $p = 0.0039$, unpaired Student's *t* test; Spindle density: GAS, $t_{(14)} = 1.930$, $p = 0.1018$; Sol, $t_{(14)} = 0.8752$, $p = 0.4151$; TA, $t_{(14)} = 0.0265$, $p = 0.9797$; EDL, $t_{(14)} = 0.5539$, $p = 0.5996$; Quad, $t_{(14)} = 3.663$, $p = 0.0105$, unpaired Student's *t* test). Double immunofluorescence staining for α-BTX and Syn/NF showed that neuromuscular junctions were intact in *Tfr1*-cKO mice, indicating that innervation might not be affected in the gastrocnemius muscle with *Tfr1* depletion (Fig. 4*D*). Bones are fundamental for movement as they help transmit the force of muscle contractions. Here, we assessed the bone morphology of a *Tfr1*-cKO mouse and a control littermate at P80 using micro-computed tomography. Serial radiographs of the *Tfr1*-cKO mouse showed no obvious deformity in the spine or hindlimb (Fig. 5*A*,*B*), indicating that *Tfr1* disruption in PV^{+} cells did not affect bone structure. These results suggested that *Tfr1* ablation in PV^{+} cells induces skeletal muscle atrophy without a concomitant effect on bone structure.

To assess whether *Tfr1* deletion in skeletal muscle contributes to the motor impairment observed in *Tfr1*-cKO mice, we delivered a Cre recombinase-dependent shRNA targeting *Tfr1* (*Tfr1*-shRNA) into adult PV-Cre mice to selectively interfere with the expression of TFR1 in PV^{+} muscle cells (Fig. 6*A*,*B*). As expected, compared with NC-shRNA injection, the administration of *Tfr1*-shRNA significantly decreased the protein level of TFR1 in skeletal muscles (Fig. 6*C*,*D*; $t_{(8)} = 2.415$, $p = 0.0422$, unpaired Student's *t* test). However, behavioral analysis showed that the latency to fall in the pole test and locomotor activity in the open field test did not differ between mice expressing *Tfr1*-shRNA in skeletal muscle and those expressing NC-shRNA (Fig. 6*E*,*F*; Falling time: $t_{(16)} = 0.4758$, $p = 0.6406$, unpaired Student's *t* test; Total distance: $t_{(16)} = 0.8340$ $p = 0.4165$, unpaired Student's *t* test). Moreover, a recent report showed that deletion of TFR1 in adult skeletal muscles did not induce spastic paraplegia (Wu et al., 2021). These results indicated that *Tfr1* deletion in PV^{+} fast muscles may not mainly contribute to the motor deficits of *Tfr1*-cKO mice.

Tfr1 deletion in PV^{+} interneurons induced axon atrophy and degeneration in the spinal cord

To identify the changes in the central nervous system that contribute to motor deficits in *Tfr1*-cKO mice, we collected whole brains and spinal cords from *Tfr1*-cKO and matched WT mice at P80. No difference was found between *Tfr1*-cKO mice and

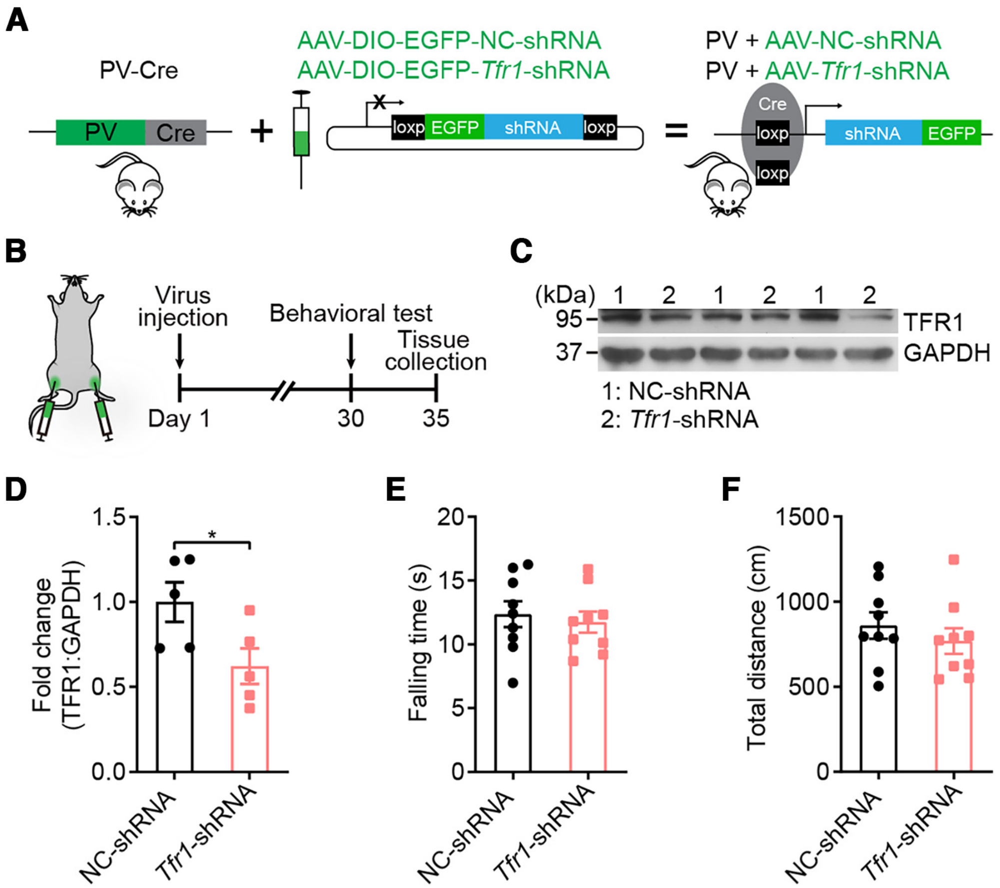

Figure 6. Skeletal muscle *Tfr1* knock-down had no effect on motor behaviors. ***A***, Schematic representation of the viral injection into PV-Cre male mice. ***B***, Schematic representation of the experimental design. ***C***, ***D***, Western blot analysis of TFR1 in skeletal muscle. $n = 5$ mice per group. ***E***, No significant difference in time to descend the pole. $n = 9$ mice per group. ***F***, Spontaneous locomotor activity of PV-Cre male mice with skeletal muscle infusions of *Tfr1*-shRNA or NC-shRNA. $n = 9$ mice per group. Data are expressed as means ± SEM; $^{*}p < 0.05$.

their WT littermates, including in gross appearance, size, and wet weight (Fig. 7*A*,*B*; Brain: $t_{(14)} = 0.6844$, $p = 0.5049$; Spinal cord: $t_{(14)} = 0.4822$, $p = 0.6329$, unpaired Student's *t* test). Images of comparable brain and spinal cord sections stained with H&E showed no obvious gross anatomic changes, including in the thickness of the corpus callosum (Fig. 7*C*–*F*; 0.90 mm: $t_{(6)} = 0.7993$, $p = 0.4546$; 0.75 mm: $t_{(6)} = 1.301$, $p = 0.2410$; 0.60 mm: $t_{(6)} = 0.1847$, $p = 0.8596$; 0.45 mm: $t_{(6)} = 1.592$, $p = 0.1625$; 0.30 mm: $t_{(6)} = 1.018$, $p = 0.3481$; 0.15 mm: $t_{(6)} = 0.8488$, $p = 0.4286$; 0.00 mm: $t_{(6)} = 1.139$, $p = 0.2980$, unpaired Student's *t* test).

We then performed immunostaining for PV in brain sections derived from motor-related or PV-enriched brain regions. Notably, the number of PV^{+} interneurons was increased in Layers II/III, IV, V, and VI of the MC, and markedly reduced in the thalamic reticular nucleus (RT) of *Tfr1*-cKO mice relative to that in WT mice (Fig. 8*A*,*B*; Cortex: Layer II/III, $t_{(10)} = 3.645$, $p = 0.0045$; Layer IV, $t_{(10)} = 2.591$, $p = 0.0269$; Layer V, $t_{(10)} = 3.093$, $p = 0.0114$; Layer VI, $t_{(10)} = 4.108$, $p = 0.0021$, unpaired Student's *t* test; RT: −0.94 mm, $t_{(10)} = 3.48$, $p = 0.0059$; −1.34 mm, $t_{(10)} = 4.512$, $p = 0.0011$; −1.82 mm, $t_{(10)} = 3.305$, $p = 0.0080$, unpaired Student's *t* test). Furthermore, the number of PV^{+} interneurons was unchanged in other brain regions, except for the somatosensory cortex (Fig. 8*C*,*D*; SC, $t_{(10)} = 3.854$, $p = 0.0032$; AuC, $t_{(10)} = 1.579$, $p = 0.1453$; VC, $t_{(10)} = 1.137$, $p = 0.2819$; Stri, $t_{(10)} = 0.357$, $p = 0.7285$; GP, $t_{(10)} = 1.154$, $p = 0.2753$; SN, $t_{(10)} = 0.1883$, $p = 0.8544$; dHip, $t_{(10)} = 0.4852$, $p = 0.6380$; vHip, $t_{(10)} = 1.194$, $p = 0.2602$, cerebellum lobule, $t_{(10)} = 1.333$, $p = 0.2309$, unpaired Student's *t* test). Studies have shown that the loss of *Tfr1* in dopaminergic neurons leads to age-related, progressive neurodegeneration in the SN, a critical structure involved in modulating motor events, thereby inducing motor deficits (Matak et al., 2016). However, immunostaining analysis showed that the number of cells in the SN that stained positive for tyrosine hydroxylase (TH), a dopaminergic neuron marker, did not differ between *Tfr1*-cKO mice and their control littermates, indicating that *Tfr1* deficiency in PV^{+} cells has little impact on dopaminergic neurons (Fig. 9; $t_{(4)} = 0.2637$, $p = 0.8051$, unpaired Student's *t* test).

Next, we investigated whether *Tfr1* deletion in brain PV^{+} interneurons affected motor regulation. To this end, we microinjected *Tfr1*-shRNA into the MC, RT, and SN of PV-Cre mice, and subjected the animals to behavioral tests 21 d after the virus injection (Fig. 10*A*). No significant differences in behavior were observed in the pole test or open field test between *Tfr1*-shRNA and their respective controls (Fig. 10*B*,*C*; Falling time: $F_{(3,23)} = 0.2$, $p = 0.8732$, one-way ANOVA; Total distance: $F_{(3,23)} = 1.1$, $p = 0.3463$, one-way ANOVA), indicating that TFR1 disruption in brain PV^{+} interneurons did not contribute to the motor deficits of *Tfr1*-cKO mice.

The spinal cord is the major conduit between the brain and the peripheral nerves, transmitting motor information from the brain to the muscles. In particular, the lumbar spinal cord is thought to directly control hindlimb movements (Ueno et al., 2018). Histologic analysis showed that, in the lumbar spinal cord, PV-tdTomato-expressing cells were mostly located in

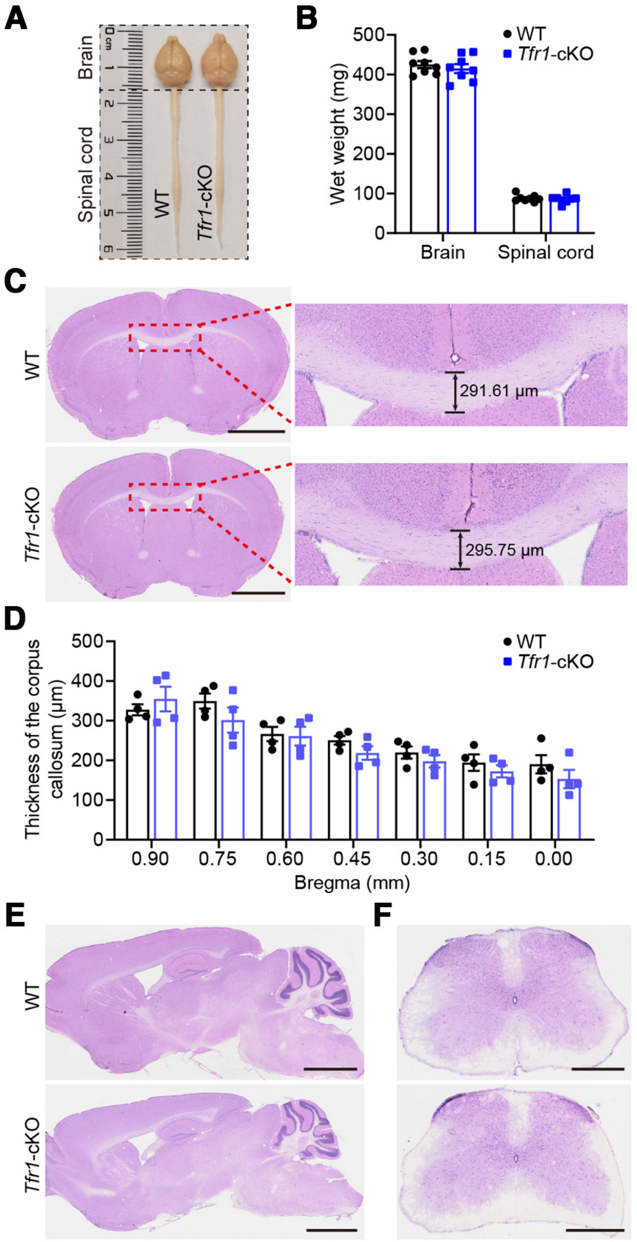

Figure 7. *Tfr1* deficiency in PV^+ neurons had no effect on brain and spinal cord architecture. ***A***, Gross appearances of the brain and spinal cord from WT and *Tfr1*-cKO male mice at P80. ***B***, Wet weight of the brain and spinal cord of WT and *Tfr1*-cKO male mice at P80. $n = 8$ mice per group. ***C***, Representative images of coronal brain sections stained with H&E. Right, Thickness of the corpus callosum in comparable brain sections. ***D***, Thickness of the corpus callosum in the brain of WT and *Tfr1*-cKO male mice at P80. $n = 4$ mice per group. ***E***, ***F***, H&E staining showed no obvious gross anatomic changes in the brain and spinal cord of WT and *Tfr1*-cKO male mice at P80. Scale bar: 2 mm (***C***, ***E***); 500 μm (***F***). Data are expressed as means ± SEM.

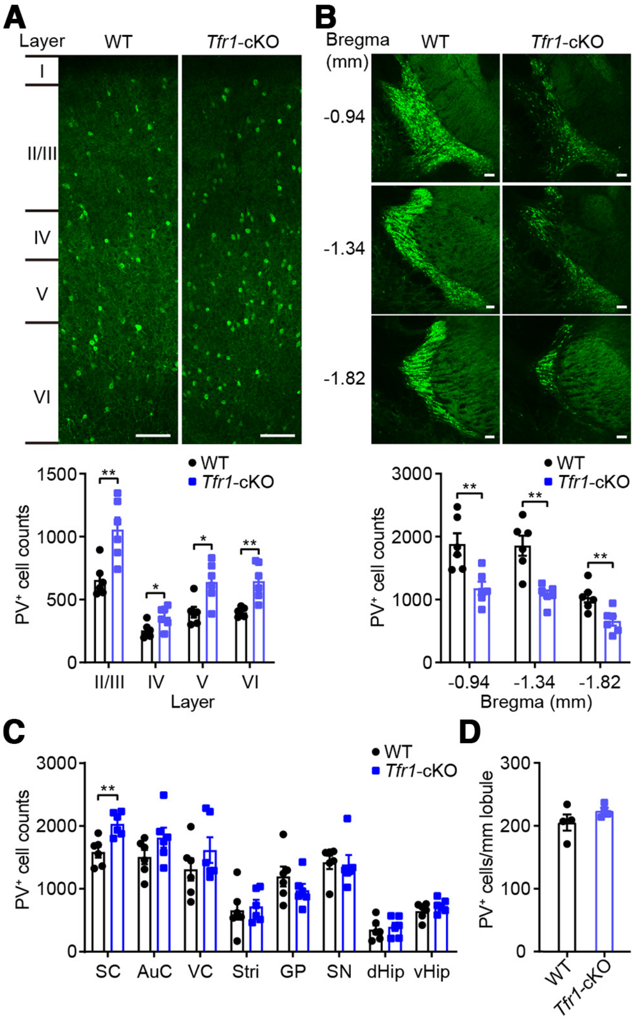

Figure 8. Changes in PV^+ interneurons in several brain regions of *Tfr1*-cKO mice. ***A***, Representative images for anti-PV immunostaining and quantification of the number of PV^+ neurons in different layers of the MC from WT and *Tfr1*-cKO male mice at P80. $n = 6$ mice per group. ***B***, Decreased number of PV^+ neurons in the RT of *Tfr1*-cKO male mice compared with WT at P80. $n = 6$ mice per group. ***C***, The number of PV^+ neurons in PV-enriched and motor-related brain areas. SC: somatosensory cortex. AuC: auditory cortex. VC: visual cortex. Stri: striatum. GP: globus pallidus. SN: substantia nigra. dHip: dorsal hippocampus. vHip: ventral hippocampus. $n = 6$ mice per group. ***D***, The density of PV^+ neurons in the cerebellum lobule of *Tfr1*-cKO and WT male mice. $n = 4$ mice per group. Scale bar: 100 μm. Data are expressed as means ± SEM; $^*p < 0.05$, $^{**}p < 0.01$.

Laminae I–IV, V, VI, and VIII (Fig. 11*A*). Anti-PV immunostaining demonstrated that the number of PV^+ neurons in the lumbar spinal cord of *Tfr1*-cKO mice was similar to that of their control littermates (Fig. 11*B*; I–IV, $t_{(8)} = 0.2964$, $p = 0.7745$; V-VI, $t_{(8)} = 0.633$, $p = 0.5444$; VIII, $t_{(8)} = 0.6871$, $p = 0.5114$, unpaired Student's *t* test). However, PV fluorescence intensity in the white matter of the dorsal spinal cord (also known as the dorsal column), which mainly includes the fasciculus gracilis and corticospinal tracts (Sahni et al., 2021), was markedly decreased in *Tfr1*-cKO mice compared with that in control animals (Fig. 11*C*). These results suggested that TFR1 ablation in PV^+ interneurons can induce axonal degeneration in the corticospinal tracts and fasciculus gracilis. To validate this possibility, we performed immunostaining for SMI-312, a pan-axonal marker, to identify the presence of axon dystrophy (Domise et al., 2019). We found that most axons in the dorsal column of the lumbar spinal cord showed anti-PV antibody staining (Fig. 11*D*,*E*), with the Mander's overlap coefficient, an indicator of co-localization, reaching 0.8845 ± 0.0083 ($n = 3$ mice). Intriguingly, compared with the controls, *Tfr1*-cKO mice exhibited a significant reduction in SMI-312 intensity (Fig. 11*F–H*; SMI-312: $t_{(50)} = 9.891$, $p < 0.0001$, unpaired Student's *t* test; PV: $t_{(50)} = 15.38$, $p < 0.0001$, unpaired Student's *t* test), a marked decrease in the number of axons, and an increase in the percentage of irregular axons in the dorsal column (Fig. 11*I–K*; Total number of axons per 100 μm^2: $t_{(62)} = 14.83$, $p < 0.0001$, unpaired Student's *t* test; Percentage of irregular axons per 100 μm^2: $t_{(62)} = 12.24$, $p < 0.0001$, unpaired Student's *t* test). To further characterize the role of TFR1 in the maintenance of PV^+ interneuron axon morphology, we prepared primary DRG neuronal cultures from P40 WT and *Tfr1*-cKO mice, as nearly one-third of DRG neurons were reported to express PV (Antal et al., 1990), and employed Sholl analysis to quantify the number of branch intersections, and determined the neurite length of PV^+ neurons using the pan-neuronal marker Tuj1 (Hou et al., 2021). As shown in Figure 11*L–N* (No. of intersections: group, $F_{(1,51)} = 31.48$, $p < 0.0001$; interaction, $F_{(796,40596)} = 9.887$, $p < 0.0001$, two-way repeated measures ANOVA; Length of the longest neurite: $t_{(51)} = 3.782$, $p = 0.0004$, unpaired Student's *t* test), DRG neurons derived from *Tfr1*-cKO mice exhibited significantly fewer branch intersections and significantly shorter neurites compared with those derived from WT mice. Together, these results support the notion that *Tfr1* deletion in PV^+ interneurons induces the degeneration of fasciculus gracilis and corticospinal tracts.

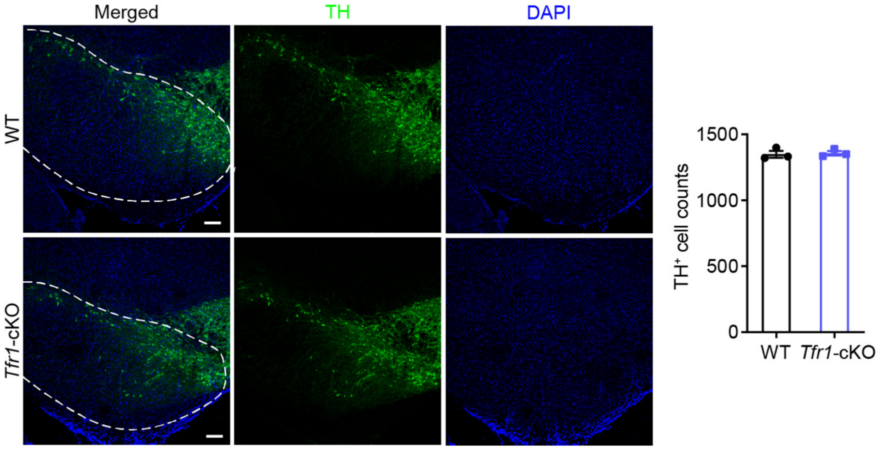

Figure 9. The number of TH^+ neurons in the SN of *Tfr1*-cKO and WT male mice at P80. Scale bar: 100 μm. $n = 3$ mice per group. Data are expressed as means ± SEM.

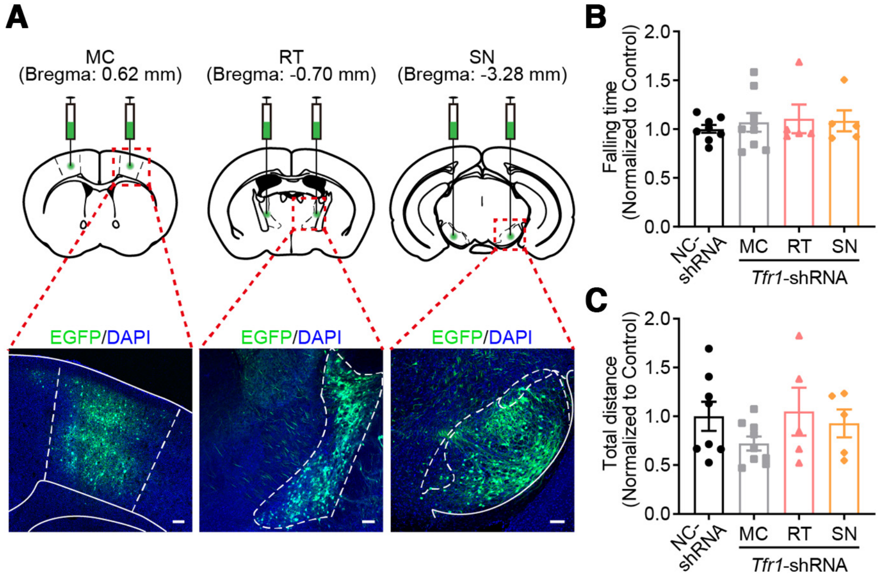

Figure 10. *Tfr1* knock-down in brain regions had little effect on motor behaviors. ***A***, Top, Injection sites in the bilateral MC, RT, and SN. Bottom, Confocal images of the brain of adult PV-Cre male mice after viral injection. ***B***, No significant differences were observed in the pole test. $n = 5–9$ mice per group. ***C***, Spontaneous locomotor activity of PV-Cre male mice with brain infusions of *Tfr1*-shRNA or NC-shRNA. $n = 5–9$ mice per group. Scale bar: 100 μm. Data are expressed as means ± SEM.

In the spinal cord, inhibitory interneurons are critical modulators of the gating of sensory inputs into motor neurons, and the postsynaptic inhibition of motor neuron excitability (Betley et al., 2009; Zhang et al., 2017). We then examined whether *Tfr1* deletion in PV^+ interneurons affects motor neurons. No difference in the number of $ChAT^+$ motor neurons in the lumbar spinal cord was observed between *Tfr1*-cKO mice and their WT littermates (Fig. 12*A*; $t_{(8)} = 0.5544$, $p = 0.5844$, unpaired Student's *t* test). However, the intensity of ChAT immunofluorescence was significantly increased, while that of PV around $ChAT^+$ motor neurons was decreased in *Tfr1*-cKO mice compared with WT animals (Fig. 12*B*,*C*; ChAT: $t_{(98)} = 6.328$, $p < 0.0001$, unpaired Student's *t* test; PV: $t_{(98)} = 8.974$, $p < 0.0001$, unpaired Student's *t* test). Moreover, Western blot results demonstrated that ChAT protein levels were significantly increased while PV protein levels were decreased in *Tfr1*-cKO mice compared with WT littermates (Fig. 12*D*,*E*; ChAT: $t_{(6)} = 4.639$, $p = 0.0035$; PV: $t_{(6)} = 2.522$, $p = 0.0452$, unpaired Student's *t* test). These results suggested that *Tfr1* deletion in PV^+ interneurons disrupts spinal circuits and, consequently, also motor output.

Tfr1 knock-down in PV^+ interneurons of the dorsal spinal cord induced motor abnormalities

To investigate whether *Tfr1* ablation in spinal cord PV^+ interneurons contributes to the motor deficits seen in *Tfr1*-cKO mice, we microinjected *Tfr1*-shRNA or NC-shRNA into the ventral lumbar spinal cord of PV-tdTomato-expressing mice (Fig. 13*A*,*B*), and subjected animals to the pole test after one month. No significant difference was recorded in the latency to descend in the pole test between the two groups (Fig. 13*C*; $t_{(10)} = 0.4959$, $p = 0.6307$, unpaired Student's *t* test), indicating that *Tfr1* downregulation in ventral spinal cord PV^+ interneurons did not affect motor coordination. We then microinjected *Tfr1*-shRNA or control shRNA into the dorsal lumbar spinal cord of PV-Cre mice (Fig. 14*A–C*), and observed that the latency to descend in the pole test increased with time following *Tfr1*-shRNA administration compared with that after NC-shRNA treatment (Fig. 14*D*; group, $F_{(1,15)} = 115.0$, $p < 0.0001$; interaction, $F_{(3,45)} = 14.29$, $p < 0.0001$, two-way repeated measures ANOVA). In addition, the FBA (Fig. 14*E*; group, $F_{(1,29)} = 27.58$, $p < 0.0001$; interaction, $F_{(3,87)} = 6.805$, $p = 0.0004$, two-way repeated measures ANOVA) and latency to fall in the rotarod test (Fig. 14*F*; group, $F_{(1,29)} = 16.78$, $p = 0.0003$; interaction, $F_{(3,87)} = 1.088$, $p = 0.3585$, two-way repeated measures ANOVA)

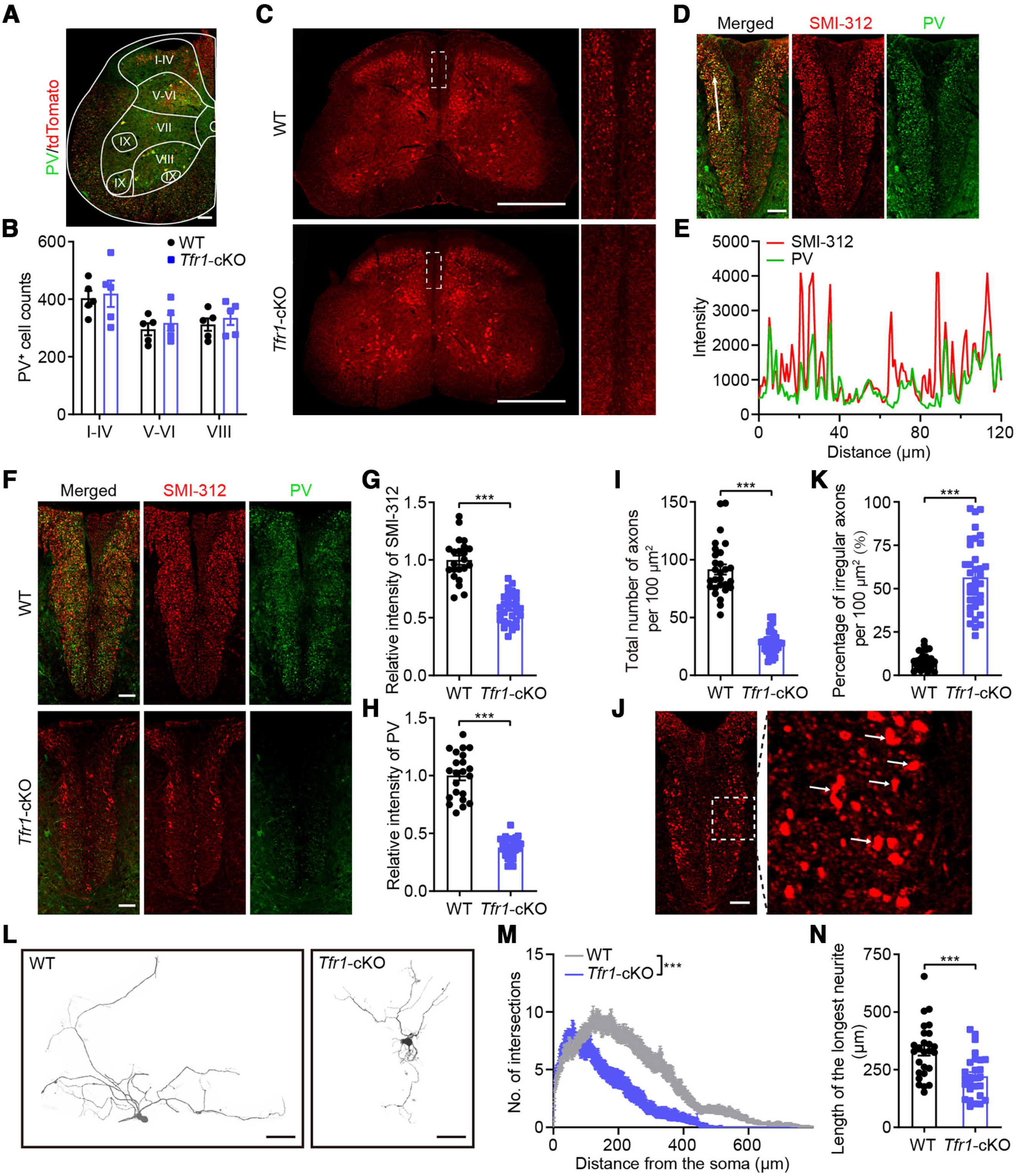

Figure 11. *Tfr1* deletion in PV$^+$ interneurons resulted in axon degeneration. ***A***, Cross-sections of the lumbar spinal cord derived from adult PV-tdTomato male mice were stained with an anti-PV antibody (green). ***B***, The number of PV$^+$ spinal cord neurons from 80-d-old WT and *Tfr1*-cKO male mice. $n = 5$ mice per group. ***C***, PV immunostaining in spinal cord sections from WT and *Tfr1*-cKO male mice at P40. ***D***, Representative coronal section immunolabeled with antibodies against SMI-312 (red) and PV (green) in the spinal cord dorsal column of a male WT mouse at P40. ***E***, Curves showing the fluorescence intensity of SMI-312 and PV marked by a white line with an arrow in ***D***. ***F***, Dystrophic axons in the spinal cord of *Tfr1*-cKO male mice at P40, as shown by SMI-312 (red) and PV (green) staining. ***G***, Quantification of the relative fluorescence intensity of SMI-312 in the dorsal column. $n = 22–30$ slices from three mice per group. ***H***, Quantification of the PV fluorescence intensity in the dorsal column. $n = 22–30$ slices from three mice per group. ***I***, Significantly decreased number of axons labeled with SMI-312 in the dorsal column of *Tfr1*-cKO female mice compared with WT. $n = 28–36$ slices from three mice per group. ***J***, Representative image showing irregular axons (marked by a white arrow) in the dorsal column of *Tfr1*-cKO female mice. Red: SMI-312. ***K***, Percentage of irregular axons labeled with SMI-312 in the dorsal column of *Tfr1*-cKO female mice compared with WT. $n = 28–36$ slices from three mice per group. ***L***, Example of an entire PV$^+$Tuj1$^+$ neuron derived from cultured DRG neurons reconstructed using Imaris software. ***M***, ***N***, Sholl analysis of *Tfr1*-cKO female mice versus their littermate controls in basal dendrites of cultured DRG PV$^+$ neurons. $n = 26–27$ neurons from three mice per group. Scale bar: 100 μm (***A***, ***L***); 500 μm (***C***); 50 μm (***D***, ***F***, ***J***). Data are expressed as means ± SEM; $^{***}p < 0.001$.

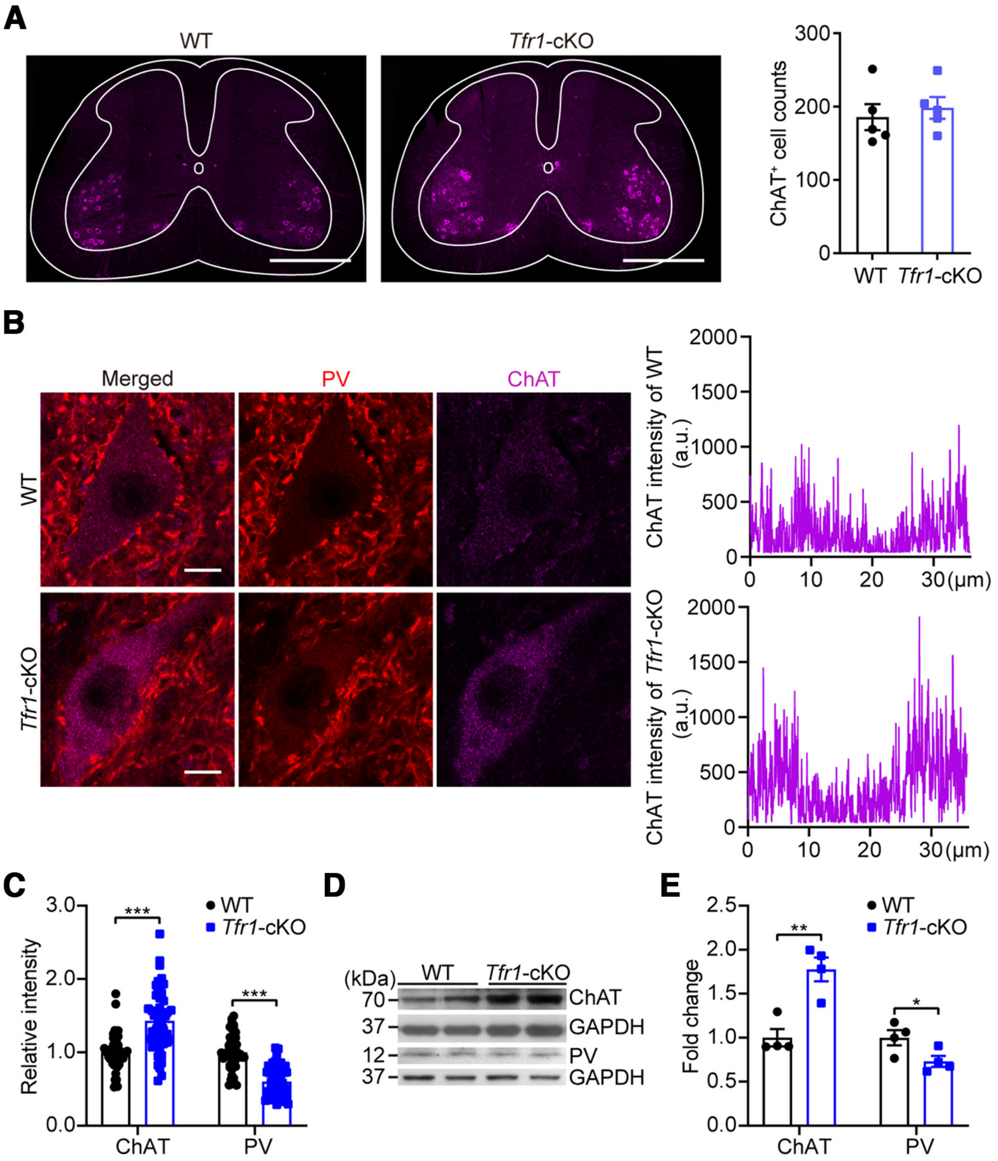

Figure 12. The expression of ChAT and PV in the ventral spinal cord of *Tfr1*-cKO mice and WT mice. ***A***, ChAT$^+$ neuron counts in the ventral spinal cord of *Tfr1*-cKO male mice compared with WT at P40. $n = 5$ mice per group. ***B***, Increased intensity of ChAT (magenta) surrounded by PV (red) terminals in the ventral spinal cord of *Tfr1*-cKO male mice compared with WT at P40. ***C***, Quantification of ChAT intensities and PV intensities around ChAT$^+$ neurons in the ventral spinal cord of *Tfr1*-cKO and WT male mice at P40. $n = 50$ neurons from five mice per group. ***D***, ***E***, Western blot analysis showed increased protein levels of ChAT and decreased protein levels of PV in the ventral spinal cord of *Tfr1*-cKO male mice compared with WT at P40. $n = 4$ mice per group. Scale bar: 500 μm (***A***); 10 μm (***B***). Data are expressed as means ± SEM; $^{**}p < 0.01$, $^{***}p < 0.001$.

were significantly lower in mice injected with *Tfr1*-shRNA than in mice of the control group. These results indicated that knocking down TFR1 in PV$^+$ interneurons in the dorsal lumbar spinal cord contributed to the impaired motor performance observed in *Tfr1*-cKO mice.

The levels of proteins related to HSP were altered in the dorsal spinal cord of *Tfr1*-cKO mice

To understand the mechanism underlying how *Tfr1* deletion in PV$^+$ interneurons in the dorsal spinal cord contributes to motor impairment, we performed a 4D label-free proteomic analysis of the dorsal lumbar spinal cord derived from 40-d-old *Tfr1*-

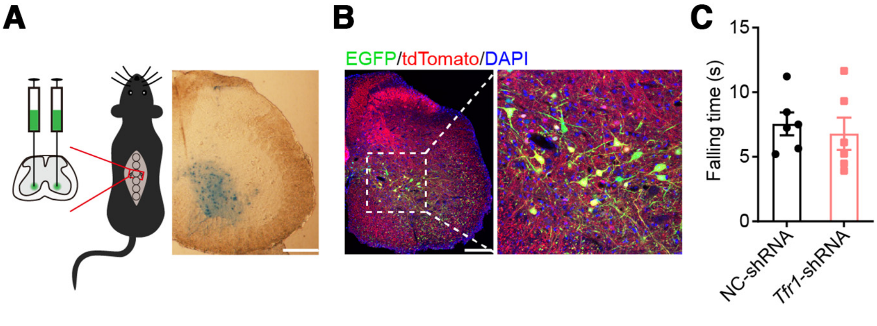

Figure 13. *Tfr1* knock-down in the PV$^+$ interneurons of ventral spinal cord had little effect on motor function. ***A***, Schematic representation of the injection site in the ventral spinal cord stained with Evans blue. ***B***, Injection sites in the ventral spinal cord of PV-tdTomato male mice with an image of EGFP expression one month after viral injection. ***C***, Time to descend the pole in the pole test one month after viral injection. $n = 6$ mice per group. Scale bar: 100 μm. Data are expressed as means ± SEM.

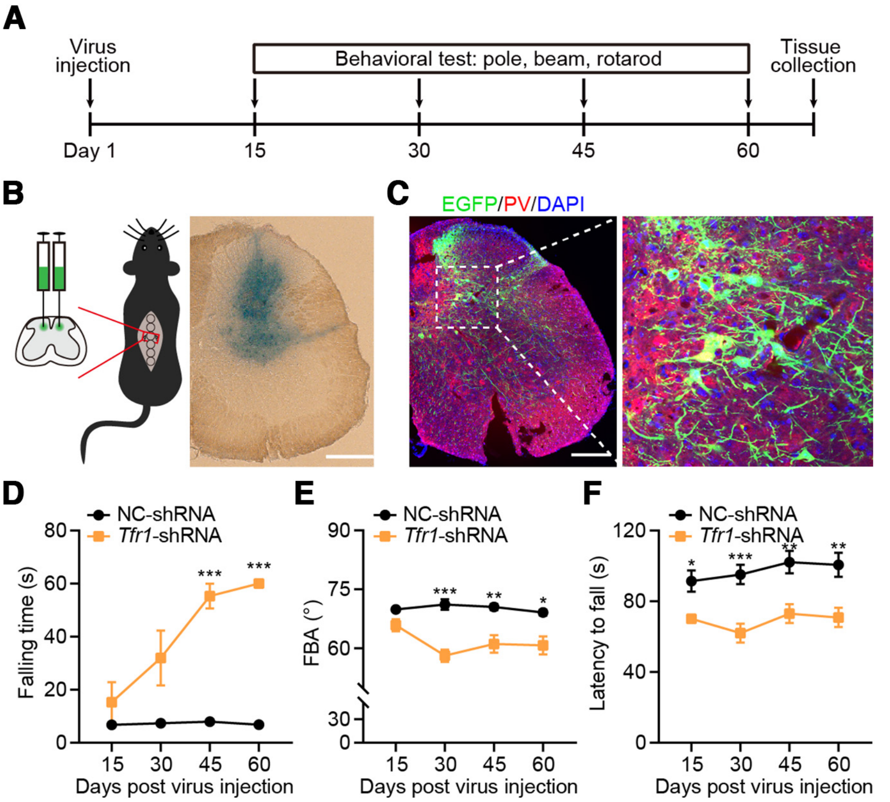

Figure 14. *Tfr1* knock-down in the PV$^+$ interneurons of dorsal spinal cord-induced motor deficits. ***A***, Experimental paradigm of the behavioral tests performed after the bilateral injection of *Tfr1*-shRNA into the dorsal spinal cord. ***B***, Schematic representation of the injection site in the dorsal spinal cord stained with Evans blue. ***C***, Validation of AAV-DIO-EGFP-*Tfr1*-shRNA (*Tfr1*-shRNA) expression in the lumbar dorsal horn. ***D***, In the pole test, the latency to descend increased with time after *Tfr1*-shRNA injection. $n = 7–10$ mice per group. ***E***, The FBA was lower in mice injected with *Tfr1*-shRNA than in mice injected with NC-shRNA. $n = 14–17$ mice per group. ***F***, The latency to fall in the rotarod test. $n = 14–17$ mice per group. Scale bar: 100 μm. Data are expressed as means ± SEM; $^*p < 0.05$, $^{**}p < 0.01$, $^{***}p < 0.001$.

cKO mice and their WT littermates. We identified 79 proteins that were differentially expressed between *Tfr1*-cKO mice and the WT controls, including 33 proteins that were significantly upregulated and 46 proteins that were downregulated in *Tfr1*-cKO animals compared with control animals. Intriguingly, 14 of the 79 proteins were related to motor disorders (Fig. 15*A*). Notably, reticulon 2 (RTN2), which has been associated with HSP (Shribman et al., 2019), was significantly downregulated in *Tfr1*-cKO mice (Fig. 15*B*). We validated the expression levels of the top 20 differentially expressed proteins and 23 HSP-related proteins using the PRM method, and found that the levels of most target proteins were consistent with those determined by proteomic analysis, validating the proteomics results. Intriguingly, the expression levels of 11 of the 23 HSP-related proteins in the spinal cord were altered following *Tfr1* deletion in PV$^+$ interneurons (Fig. 15*C*; Rtn2, $t_{(4)}$ = 19.24, $q < 0.0001$; Kif1a, $t_{(4)}$ = 6.099, $q = 0.0090$; Ddhd2, $t_{(4)}$ = 11.41, $q = 0.0012$; Bicd2, $t_{(4)}$ = 12.66, $q = 0.0010$; Spg21, $t_{(4)}$ = 3.664, $q = 0.0369$; Spast, $t_{(4)}$ = 2.773, $q = 0.0783$; L1cam, $t_{(4)}$ = 19.05, $q = 0.0004$; Ampd2, $t_{(4)}$ = 4.166, $q = 0.0269$; Fa2h, $t_{(4)}$ = 5.19, $q = 0.0141$; Cpt1c, $t_{(4)}$ = 9.648, $q = 0.0018$; Reep2, $t_{(4)}$ = 12.44, $q = 0.0010$; Klc2, $t_{(4)}$ = 2.619, $q = 0.0843$; Kif5a, $t_{(4)}$ = 0.414, $q = 0.6141$; Spg7, $t_{(4)}$ = 1.651, $q = 0.2134$; Gba2, $t_{(4)}$ = 0.2828, $q = 0.6176$; Ubap1, $t_{(4)}$ = 1.253, $q = 0.2812$; Tmed9, $t_{(4)}$ = 1.412, $q = 0.2588$; Vps28, $t_{(4)}$ = 0.0877, $q = 0.6975$; Sacs, $t_{(4)}$ = 2.042, $q = 0.1462$; Bscl2, $t_{(4)}$ = 1.375, $q = 0.2859$; Reep1, $t_{(4)}$ = 0.4867, $q = 0.6141$; Kif1c, $t_{(4)}$ = 0.3916, $q = 0.6141$; Ddhd1, $t_{(4)}$ = 0.3277, $q = 0.6176$, multiple two-tailed *t* tests following FDR correction).

Next, we performed *in vitro* experiments, and found that incubation with $Fe(NH_4)_2(SO_4)_2$ could lower TFR1 levels in primary cultured neurons (Fig. 16*B*), consistent with a previous report (Duce et al., 2010). Then, we prepared primary DRG neuronal cultures from PV-tdTomato mice and analyze the morphology of PV-tdTomato$^+$ and PV-tdTomato$^-$ neurons after $Fe(NH_4)_2(SO_4)_2$ application. Axon degeneration was evident in PV$^+$ neurons, but not in PV$^-$ neurons, indicating that iron homeostasis is essential for dendrite maintenance in PV$^+$ interneurons (Fig. 16*A*,*C–F*; PV-tdTomato$^+$ neurons: no. of intersections: group, $F_{(1,50)}$ = 12.63, $p = 0.0008$; interaction, $F_{(1050,52500)}$ = 2.824, $p < 0.0001$, two-way repeated measures ANOVA; length of the longest neurite: $t_{(50)}$ = 2.753, $p = 0.0082$, unpaired Student's *t* test; PV-tdTomato$^-$ neurons: no. of intersections: group, $F_{(1,38)}$ = 1.532, $p = 0.2234$; interaction, $F_{(769,29222)}$ = 1.069, $p = 0.0937$, two-way repeated measures ANOVA; length of the longest neurite: $t_{(38)}$ = 1.715, $p = 0.0945$, unpaired Student's *t* test). Intriguingly, we found that the expression levels of 17 of the 23 HSP-related proteins were altered following treatment with $Fe(NH_4)_2(SO_4)_2$ compared with that in vehicle-treated neurons (Fig. 16*G*; Rtn2, $t_{(4)}$ = 11.31, $q = 0.0025$; Kif1a, $t_{(4)}$ = 2.969, $q = 0.0364$; Ddhd2, $t_{(4)}$ = 7.444, $q = 0.0047$; Bicd2, $t_{(4)}$ = 5.98, $q = 0.0079$; Spg21, $t_{(4)}$ = 7.155, $q = 0.0048$; Spast, $t_{(4)}$ = 3.332, $q = 0.0274$; L1cam, $t_{(4)}$ = 4.009, $q = 0.0180$; Ampd2, $t_{(4)}$ = 4.279, $q = 0.0165$; Fa2h, $t_{(4)}$ = 0.5285, $q = 0.4490$; Cpt1c, $t_{(4)}$ = 0.908, $q = 0.3262$; Klc2, $t_{(4)}$ = 3.974, $q = 0.0180$; Kif5a, $t_{(4)}$ = 29.4, $q = 0.0001$; Spg7, $t_{(4)}$ = 9.093, $q = 0.0038$; Gba2, $t_{(4)}$ = 4.772, $q = 0.0125$; Ubap1, $t_{(4)}$ = 7.941, $q = 0.0048$; Tmed9, $t_{(4)}$ = 4.873, $q = 0.0125$; Vps28, $t_{(4)}$ = 2.805, $q = 0.0404$; Sacs, $t_{(4)}$ = 3.44, $q = 0.0265$; Bscl2, $t_{(4)}$ = 4.915, $q = 0.0125$; Reep1, $t_{(4)}$ = 0.5128, $q = 0.4490$, multiple two-tailed *t* tests following FDR correction). Notably, five HSP-related proteins showed the same expression tendency *in vivo* and *in vitro* (Figs. 15*C*, 16*G*). Combined with the features of *Tfr1*-cKO mice, these results indicated that iron deficiency in PV$^+$ interneurons induces a HSP-like phenotype.

Intracerebroventricular infusion of DFP induced motor deficits in adult mice

To determine whether *Tfr1* knock-out induces iron deficiency, we first detected iron concentrations. No differences in serum iron levels were found between *Tfr1*-cKO mice and control littermates (Fig. 17*A*; $t_{(18)}$ = 0.4119, $p = 0.6853$, unpaired Student's *t* test). However, in the dorsal spinal cord, the iron levels were significantly lower in *Tfr1*-cKO mice than in those of WT littermates (Fig. 17*B*; $t_{(18)}$ = 2.648, $p = 0.0164$, unpaired Student's *t* test). Moreover, *Ftl* and *Irp1* mRNA levels were markedly decreased in the spinal cord of *Tfr1*-cKO mice compared with WT controls (Fig. 17*C*; *Fth*: $t_{(9)}$ = 0.2387, $p = 0.8167$; *Ftl*: $t_{(9)}$ = 4.231, $p = 0.0022$; *Slc11a2*: $t_{(9)}$ = 0.5758, $p = 0.5788$; *Irp1*:

$t_{(9)}$ = 2.758, $p = 0.0222$; *Irp2*: $t_{(9)}$ = 0.1020, $p = 0.9210$; *Tfr1*: $t_{(9)}$ = 0.1036, $p = 0.9197$, unpaired Student's *t* test). We then assessed whether iron deficit in the spinal cord affects motor function. To this end, we infused DFP, a well-documented iron chelator which coordinates with free iron (Sohn et al., 2008), into the lateral ventricle of adult C57BL/6J mice (Fig. 18*A*). We found that infusion of DFP time-dependently increased the latency to descend in the pole test and decreased the FBA in the beam balance test and the latency to fall in the rotarod test (Fig. 18*B–D*; Falling time: group, $F_{(1,14)} = 7.564$, $p = 0.0156$; interaction, $F_{(3,42)} = 6.337$, $p = 0.0012$, two-way repeated measures ANOVA; FBA: group, $F_{(1,14)}$ = 6.528, $p = 0.0229$; interaction, $F_{(3,42)}$ = 5.302, $p = 0.0034$, two-way repeated measures ANOVA; Latency to fall: group, $F_{(1,27)}$ = 5.610, $p = 0.0253$; interaction, $F_{(3,81)}$ = 3.377, $p = 0.0222$, two-way repeated measures ANOVA). In addition, no marked change in the morphology or weight of skeletal muscle was found between DFP-treated and control mice (Fig. 18*E*,*F*; GAS, $t_{(11)}$ = 0.3362, $p = 0.7430$; Sol, $t_{(11)}$ = 0.6632, $p = 0.5208$; TA, $t_{(11)} = 0.1422$, $p = 0.8895$; EDL, $t_{(11)}$ = 2.184, $p = 0.0515$; Quad, $t_{(11)}$ = 0.1373, $p = 0.8933$, unpaired Student's *t* test). Also, no difference in the cross-sectional area or the diameter of cells in the quadriceps muscle fibers was observed between the two groups (Fig. 18*G–I*; Cross-sectional area: $t_{(6)} = 0.4724$, $p = 0.6533$, unpaired Student's *t* test; Cell diameter: $t_{(6)}$ = 0.000, $p > 0.9999$, unpaired Student's *t* test). Intriguingly, axonal loss in the dorsal column also occurred as evidenced by a decrease in SMI-312 and PV immunofluorescence in the dorsal column of DFP-treated animals relative to that in vehicle-treated controls (Fig. 18*J–L*; SMI-312: $t_{(110)}$ = 12.36, $p < 0.0001$, unpaired Student's *t* test; PV: $t_{(110)} = 17.80$, $p < 0.0001$, unpaired Student's *t* test). These results were consistent with those obtained for *Tfr1*-cKO mice, indicating that iron deficiency in the nervous system, especially spinal cord, leads to motor deficits and axon degeneration in PV^+ interneurons in adult mice.

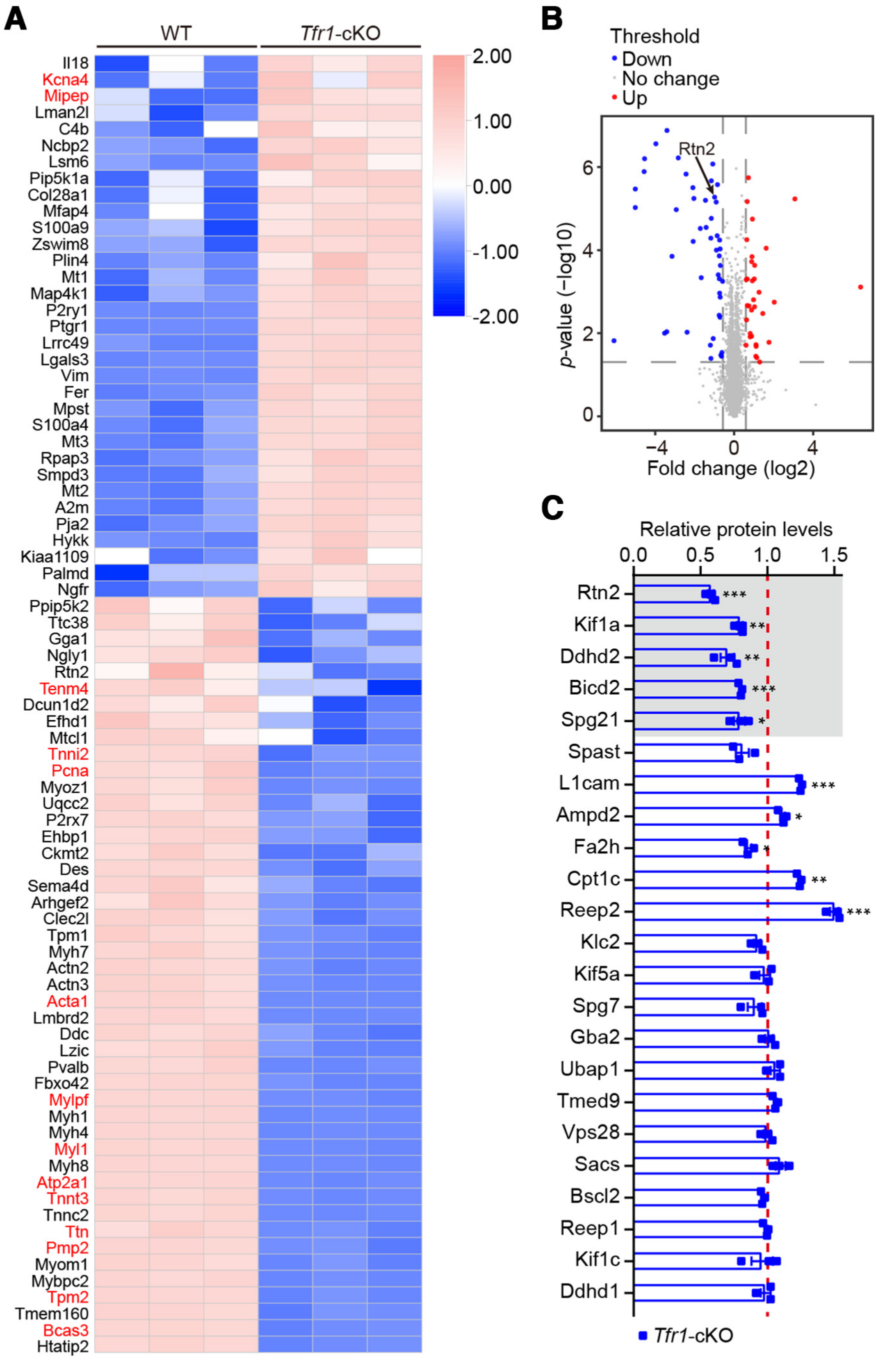

Figure 15. The expression of HSP-related proteins was altered in the dorsal spinal cord of *Tfr1*-cKO mice. ***A***, Heatmap of the differentially expressed proteins between *Tfr1*-cKO male mice and their control littermates. Proteins shown in red are related to motor disorders. ***B***, Volcano plot depicting the differentially expressed proteins in *Tfr1*-cKO mice. Red dots represent significantly upregulated proteins in *Tfr1*-cKO mice and blue dots represent significantly downregulated proteins. ***C***, PRM results for HSP-related proteins in the spinal cord of *Tfr1*-cKO male mice compared with their WT littermates. WT, red dashed line. $n = 3$ mice per group. Data are expressed as means ± SEM; $^*p < 0.05$, $^{**}p < 0.01$, $^{***}p < 0.001$.

Iron repletion partially rescued the motor deficits of *Tfr1*-cKO mice

To investigate whether iron repletion can rescue the phenotypes of *Tfr1*-cKO mice, we administered iron dextran intraperitoneally into *Tfr1*-cKO mice and their control littermates at P10 and P20, respectively, and analyzed their behavior at P40 and P60 (Fig. 19*A*). After treatment with iron dextran, *Tfr1*-cKO mice showed a significantly shorter latency to descend in the pole test (Fig. 19*B*; P40: group, $F_{(1,50)}$ = 15.22, $p = 0.0003$; interaction, $F_{(1,50)} = 5.047$, $p = 0.0291$; P60: group, $F_{(1,50)} = 44.29$, $p < 0.0001$; interaction, $F_{(1,50)} = 21.60$, $p < 0.0001$, two-way ANOVA), and a significantly higher FBA in the beam test and latency to fall off in the rotarod test (Fig. 19*C*,*D*; FBA: P40, group, $F_{(1,50)} = 42.67$, $p <$ 0.0001; interaction, $F_{(1,50)}$ = 5.194, p = 0.0270; P60, group,

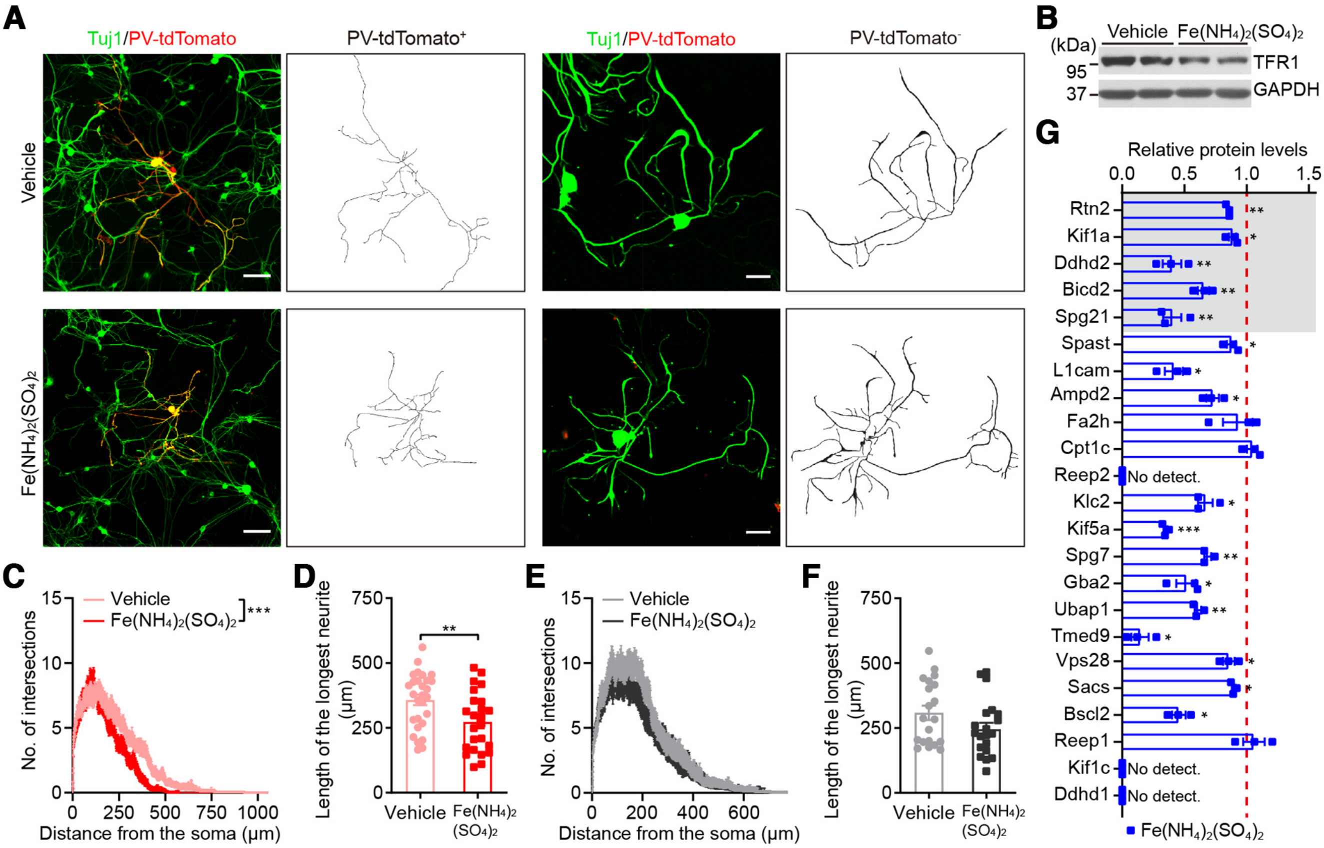

Figure 16. $Fe(NH_4)_2(SO_4)_2$ application induced axon degeneration in PV^+ neurons. ***A***, Representative images of $tdTomato^+$ and $tdTomato^-$ neurons co-stained with Tuj1 (green) 24 h after $Fe(NH_4)_2(SO_4)_2$ (75 mM) treatment and traces of dendritic arbors generated using Imaris software. ***B***, Western blotting showing that the expression of TFR1 was lower in primary cultured DRG neurons treated with $Fe(NH_4)_2(SO_4)_2$ than in those treated with vehicle. ***C***, ***D***, Sholl analysis of PV-$tdTomato^+$ neurons treated with $Fe(NH_4)_2(SO_4)_2$ or vehicle. $n = 24–28$ neurons per group. ***E***, ***F***, Sholl analysis of PV-$tdTomato^-$ neurons treated or not with $Fe(NH_4)_2(SO_4)_2$ or vehicle. $n = 20$ neurons per group. ***G***, Changes in the expression levels of HSP-related proteins following $Fe(NH_4)_2(SO_4)_2$ treatment as determined by PRM. Vehicle, red dashed line. $n = 3$ mice per group. The gray shaded area in ***G*** indicates proteins with the same change in expression as that shown in Figure 15*C*. Scale bar: 100 μm. Data are expressed as means ± SEM; $*p < 0.05$, $**p < 0.01$, $***p < 0.001$.

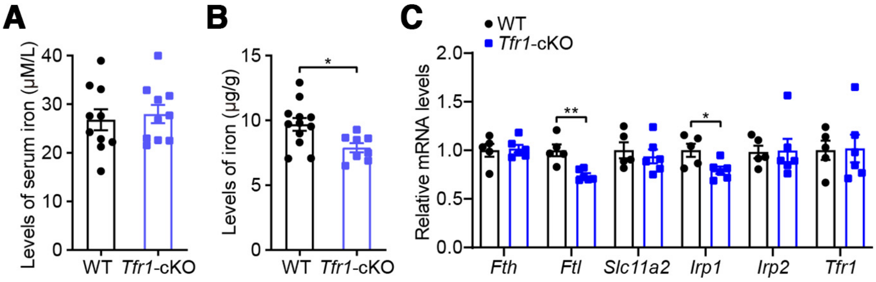

Figure 17. Disruption of iron homeostasis in the dorsal spinal cord of *Tfr1*-cKO mice. ***A***, Serum iron. $n = 10$ mice per group. ***B***, Iron concentrations in the dorsal spinal cord of *Tfr1*-cKO and WT male mice at P40. $n = 8–12$ mice per group. ***C***, Relative mRNA levels of proteins involved in cellular iron metabolism in the dorsal spinal cord of *Tfr1*-cKO and WT male mice at P40. $n = 5–6$ mice per group. Data are expressed as means ± SEM; $*p < 0.05$, $**p < 0.01$.

$F_{(1,50)} = 51.24$, $p < 0.0001$; interaction, $F_{(1,50)} = 10.06$, $p = 0.0026$, two-way ANOVA; Latency to fall: P40, group, $F_{(1,50)} = 11.86$, $p = 0.0012$; interaction, $F_{(1,50)} = 1.797$, $p = 0.1862$; P60, group, $F_{(1,50)} = 33.63$, $p < 0.0001$; interaction, $F_{(1,50)} = 5.789$, $p = 0.0199$, two-way ANOVA) compared with that for PBS-treated mice. Moreover, axon loss induced by *Tfr1* deletion in PV^+ interneurons was partially rescued in the dorsal column after iron repletion (Fig. 19*E–G*; SMI-312: group, $F_{(1,177)} = 357.9$, $p < 0.0001$; interaction, $F_{(1,177)} = 8.771$, $p = 0.0035$, two-way ANOVA; PV: group, $F_{(1,177)} = 391.5$, $p < 0.0001$; interaction, $F_{(1,177)} = 77.05$, $p < 0.0001$, two-way ANOVA). These results indicated that iron repletion partly reversed motor deficits and axon degeneration in *Tfr1*-cKO mice.

Discussion

In this study, we excised floxed *Tfr1* using Cre recombinase expressed under the control of the PV promoter to determine the potential role of iron metabolism in PV^+ interneurons. We found that (1) *Tfr1*-cKO mice developed early-onset, progressive motor deficits characterized by lower-limb spasticity and slight cognitive impairment; (2) *Tfr1*-cKO mice exhibited skeletal muscle atrophy and axon degeneration in the spinal cord dorsal column; (3) *Tfr1* knockdown specifically in dorsal spinal cord PV^+ interneurons induced motor deficits, as did DFP-mediated iron chelation; (4) several proteins previously associated with motor disorders were differentially expressed in the dorsal spinal cord of *Tfr1*-cKO mice; and (5) treatment with iron dextran partly rescued the behavioral phenotypes and neuronal morphology in *Tfr1*-cKO mice. Our study describes a new mouse model suitable for mechanistic and therapeutic studies of motor disorders, especially HSP, and provides novel insights into iron metabolism in spinal cord PV^+ interneurons, and its role in the regulation of motor functions.

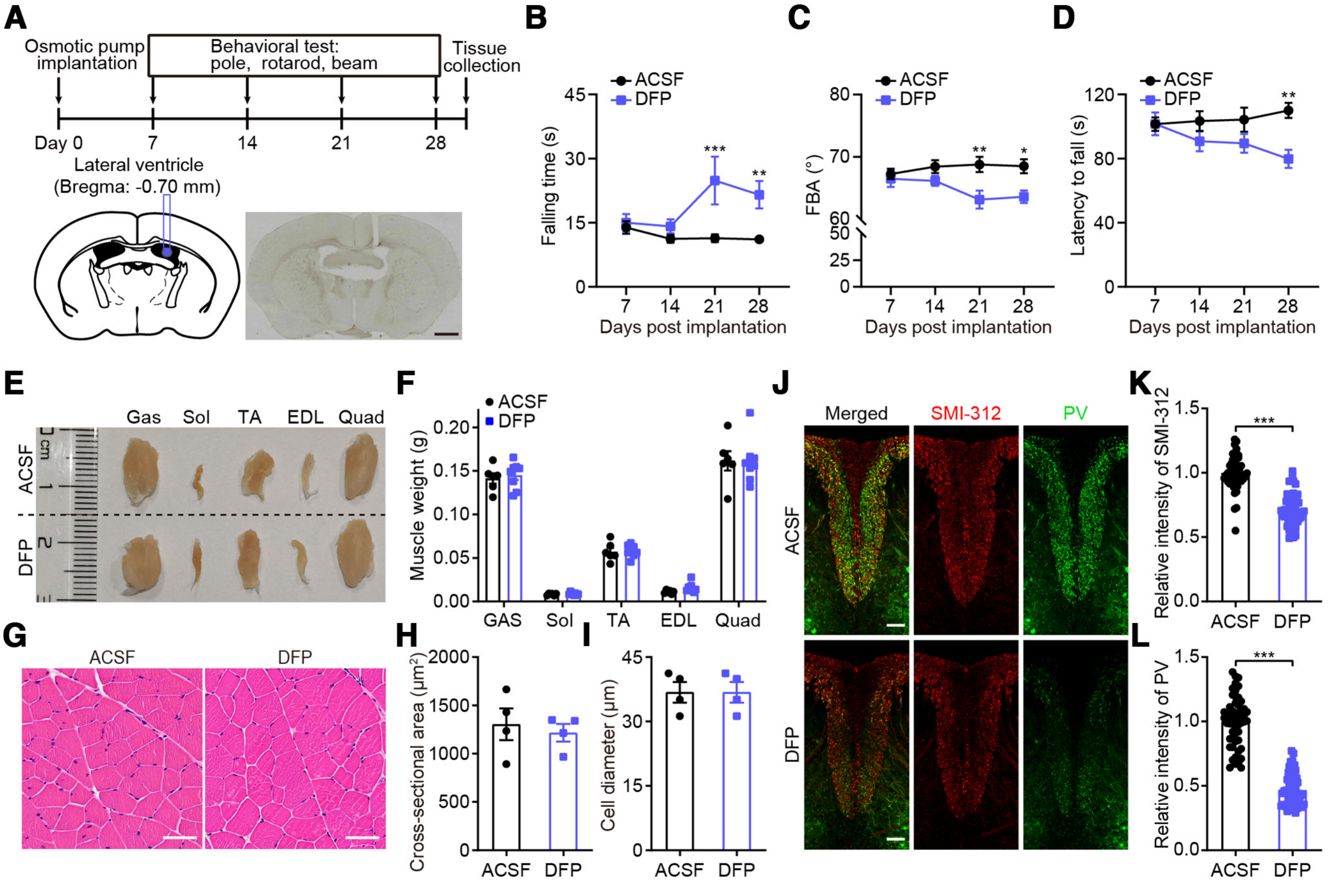

Figure 18. Infusion of DFP induced motor deficits in adult C57BL/6J male mice. ***A***, Top, Experimental paradigm for the behavioral tests performed after DFP infusion. Bottom, A representative image showing osmotic pump implantation into the right lateral ventricle. ***B***, The latency to descend in the pole test increased with time post-DFP infusion compared with control animals. $n = 7–9$ mice per group. ***C***, The FBA was lower in DFP-treated mice than in ACSF-treated mice. $n = 7–9$ mice per group. ***D***, The latency to fall in the rotarod test decreased after DFP infusion. $n = 14–15$ mice per group. ***E***, ***F***, Comparison of the morphology and wet weight of skeletal muscle between DFP-infused and ACSF-infused mice. $n = 6–7$ mice per group. ***G–I***, H&E staining of transectioned quadriceps muscle fibers showed no difference in fiber area or cell diameter between the two groups. $n = 4$ mice per group. ***J***, Axons in the spinal cords of DFP-infused mice and control mice immunostained for SMI-312 (red) and PV (green). ***K***, Quantification of SMI-312 fluorescence intensity in the dorsal column. $n = 54–58$ slices from four mice per group. ***L***, Quantification of PV fluorescence intensity in the dorsal column. $n = 54–58$ slices from four mice per group. Scale bar: 1 mm (***A***); 50 μm (***G***, ***J***). Data are expressed as means ± SEM; $*p < 0.05$, $**p < 0.01$, $***p < 0.001$.

HSP is a rare neurodegenerative disorder characterized by progressive spasticity and weakness of the lower limbs. In this study, we found that *Tfr1*-cKO mice displayed obvious spastic-like tremors in the hindlimb, motor deficits, and mild cognitive impairment in *Tfr1*-cKO mice at P40, effects that worsened with age and manifested more severely in males than in females. These behavioral features are very similar to the core clinical symptoms of HSP, a significant male predominance disease (Schüle et al., 2016). Our histologic analysis indicated that skeletal muscle atrophy was present in *Tfr1*-cKO mice at P80, possibly because of long-lasting spastic paraplegia (Kern et al., 2008). Spinal cord neurons are the neurons most severely affected by HSP (Salinas et al., 2008). Here, we found that *Tfr1*-cKO mice exhibited axon degeneration in the lumbar spinal cord dorsal column, including in the fasciculus gracilis and corticospinal tracts, which is consistent with the most prominent neuropathological signs of HSP (Fink, 2013). Studies have demonstrated that a high-iron diet can alter the expression of genes involved in HSP, such as spastin (*SPAST*; Johnstone and Milward, 2010). Genotype strongly correlates with neurodegeneration with brain iron accumulation and motor illnesses, particularly for HSP-associated genes such as chromosome 9 open reading frame 72 (*C9orf72*), fatty acid 2-hydroxylase (*FA2H*), and ATPase cation transporting 13A2 (*ATP13A2*; Boutry et al., 2019). Moreover, in the present study, using proteomics and a PRM approach, we found that the expression of several HSP-related proteins, including RTN2, kinesin family member 1A (KIF1A), DDHD domain containing 2 (DDHD2), bicaudal D homolog 2 (BICD2), and spastic paraplegia 21 protein (SPG21), was significantly decreased both *in vivo* and *in vitro*. Mutations in the genes that encode the above-mentioned proteins have been reported to result in different HSP subtypes. For instance, mutations in *RTN2*, encoding a prototypic ER-shaping protein that interacts with spastin, lead to abnormal ER morphogenesis and are responsible for the spastic paraplegia 12 subtype of HSP (Montenegro et al., 2012). Mutations in the *KIF1A* gene are responsible for the SPG30 subtype, which is characterized by the onset of spastic gait and hyperreflexia of the lower limbs in the first or second decade of life (Klebe et al., 2012). Meanwhile, mutations in *DDHD2*, which encodes an intracellular phospholipase A1 with phospholipase and lipase activities, cause a complex HSP subtype (SPG54), with a core phenotype that consists of very early-onset (less than two years) spastic paraplegia and intellectual disability (Schuurs-Hoeijmakers et al., 2012). Pathogenic variants of *BICD2*, which encodes BICD2, a dynein–dynactin trafficking adaptor protein, lead to dominant congenital spinal

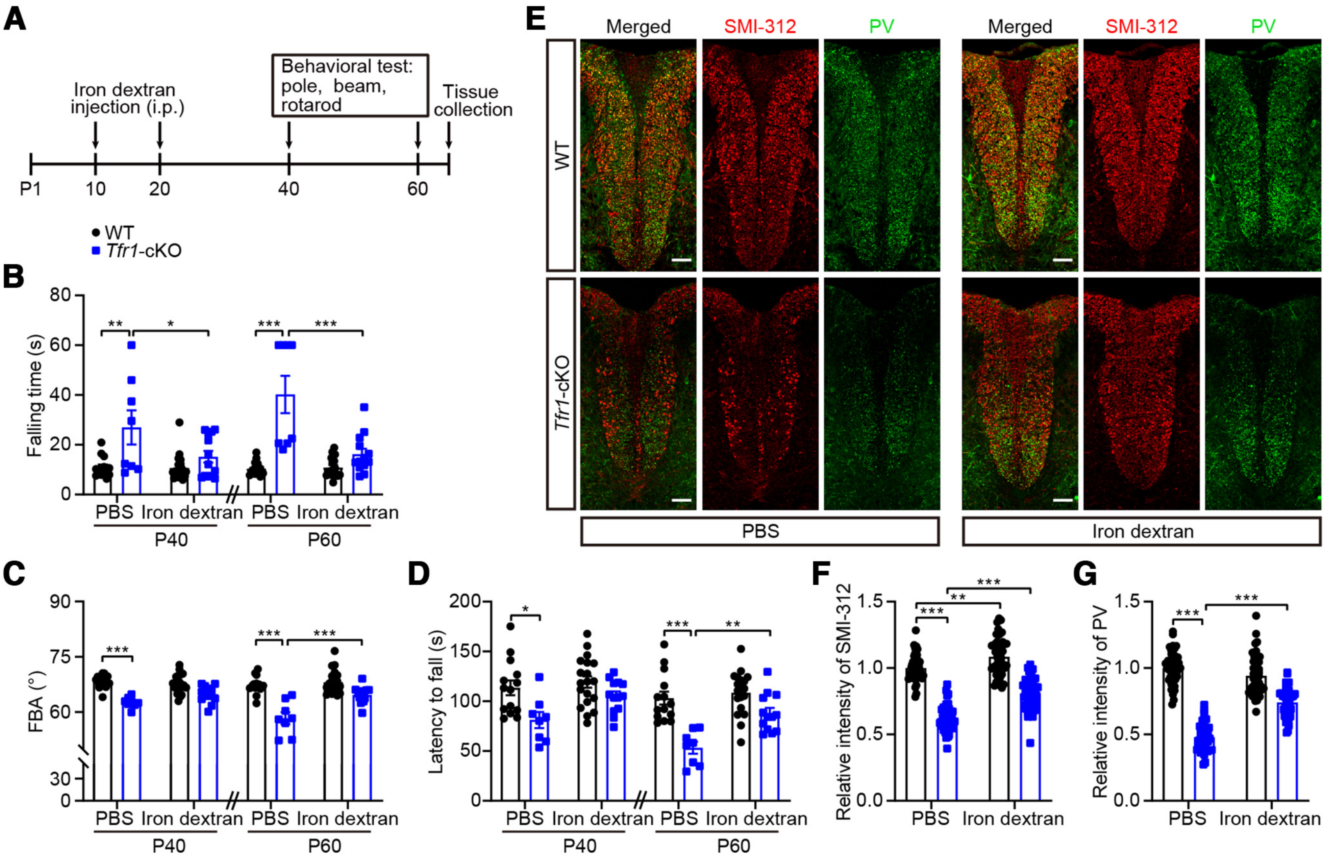

Figure 19. Iron dextran partly rescued motor deficits and axon loss in *Tfr1*-cKO mice. ***A***, Experimental paradigm for the behavioral tests performed after iron dextran treatment. ***B***, Latency to descend in the pole test after iron dextran treatment in male and female *Tfr1*-cKO mice. $n = 8–19$ mice per group; male: 5–10 mice per group; female: 3–9 mice per group. ***C***, The FBA in the beam test after iron dextran treatment. $n = 8–19$ mice per group; male: 5–10 mice per group; female: 3–9 mice per group. ***D***, Latency to fall in the rotarod test after iron dextran treatment. $n = 8–19$ mice per group; male: 5–10 mice per group; female: 3–9 mice per group. ***E***, Representative images of SMI-312 (red) and PV (green)-stained axons in the dorsal column of the spinal cord. ***F***, Quantification of SMI-312 fluorescence intensity in the dorsal column. $n = 41–49$ slices from four male mice per group. ***G***, Quantification of PV fluorescence intensity in the dorsal column. $n = 41–49$ slices from four male mice per group. Scale bar: 50 μm. Data are expressed as means ± SEM; $^{*}p < 0.05$, $^{**}p < 0.01$, $^{***}p < 0.001$.

muscular atrophy and HSP (Oates et al., 2013). Finally, the SPG21 subtype, also known as Mast syndrome, was demonstrated to be a complicated form of HSP associated with dementia, and is characterized by major feature onset in early adulthood (Simpson et al., 2003). The clinical features resulting from mutations in HSP-related genes, such as early onset and cognitive impairment, are highly consistent with the phenotypes observed in *Tfr1*-cKO mice in our study. Indeed, the motor phenotype and the morphologic and molecular changes seen in *Tfr1*-cKO mice recapitulate the major behavioral and neuropathological characteristics of HSP.

Spinal interneurons are crucial modulators of motor functions (Catela et al., 2015; Zhang et al., 2017). Interneurons in Laminae V and VI can directly project onto motor neurons in the ventral spinal cord (Osseward and Pfaff, 2019), while motor neurons constitute the final efferent pathway of muscles. PV^+ interneurons mainly distributed in Laminae I–VI and VIII in the spinal cord (Fig. 11*A*), effectively control network excitability. Iron deficiency severely impacts PV expression (Callahan et al., 2013; Bastian et al., 2014), which can affect the electrophysiological properties of PV^+ interneurons. In our study, we observed an increase in the fluorescence intensity of ChAT and a decrease in that of PV around $ChAT^+$ motor neurons in the ventral spinal cord of *Tfr1*-cKO mice. The functional consequences of these changes include reduced inhibitory transmission in the spinal cord. These data suggested that iron deficiency in PV^+ interneurons leads to disrupted spinal circuits, which may affect motor output. In addition, we identified several proteins with altered expression in the dorsal lumbar spinal cord of *Tfr1*-cKO mice that have previously been associated with motor disorders, especially HSP (Salinas et al., 2008; Blackstone, 2012). These changed proteins function in several pathways, including those involved in membrane trafficking, axonal transport, mitochondrial function, endosomal dynamics and lipid synthesis and metabolism (Blackstone, 2012). When altered, these pathways can promote axonal degeneration in the spinal cord and lead to motor impairments.

Treatment with iron dextran partly rescued the phenotype of *Tfr1*-cKO mice, further indicating that iron metabolism has a major role in movement control, and may thus serve as a target for the treatment of motor disorders. A shear-thinning, ROS-scavenging hydrogel combined with dental pulp stem cells effectively reduced muscle spasms and promoted spinal cord repair by improving vascular function and regulating iron metabolism (Ying et al., 2023). Moreover, iron-related preparations are widely used in clinical practice. Various forms of iron supplements commonly used therapeutically are inexpensive and safe, thus providing a good clinical basis for their application in motor disorders. While this study focused on a very rare neuropathy, iron metabolism has been implicated in an expanding number of motor diseases (Rouault, 2013; Ward et al., 2014; Tseng et al., 2018). Our findings highlight the therapeutic potential of targeting iron metabolism for preventing or delaying the development and progression of motor disorders, especially HSP.

References

Antal M, Freund TF, Polgár E (1990) Calcium-binding proteins, parvalbumin- and calbindin-D 28k-immunoreactive neurons in the rat spinal cord and dorsal root ganglia: a light and electron microscopic study. J Comp Neurol 295:467–484.

Barrientos T, Laothamatas I, Koves TR, Soderblom EJ, Bryan M, Moseley MA, Muoio DM, Andrews NC (2015) Metabolic catastrophe in mice lacking transferrin receptor in muscle. EBioMedicine 2:1705–1717.

Bastian TW, Prohaska JR, Georgieff MK, Anderson GW (2014) Fetal and neonatal iron deficiency exacerbates mild thyroid hormone insufficiency effects on male thyroid hormone levels and brain thyroid hormone-responsive gene expression. Endocrinology 155:1157–1167.

Betley JN, Wright CVE, Kawaguchi Y, Erdélyi F, Szabó G, Jessell TM, Kaltschmidt JA (2009) Stringent specificity in the construction of a GABAergic presynaptic inhibitory circuit. Cell 139:161–174.

Blackstone C (2012) Cellular pathways of hereditary spastic paraplegia. Annu Rev Neurosci 35:25–47.

Boutry M, Morais S, Stevanin G (2019) Update on the genetics of spastic paraplegias. Curr Neurol Neurosci 19:18.

Callahan LSN, Thibert KA, Wobken JD, Georgieff MK (2013) Early-life iron deficiency anemia alters the development and long-term expression of parvalbumin and perineuronal nets in the rat hippocampus. Dev Neurosci 35:427–436.

Catela C, Shin MM, Dasen JS (2015) Assembly and function of spinal circuits for motor control. Annu Rev Cell Dev Biol 31:669–698.

Chen AC, Donovan A, Ned-Sykes R, Andrews NC (2015) Noncanonical role of transferrin receptor 1 is essential for intestinal homeostasis. Proc Natl Acad Sci U S A 112:11714–11719.

Chen WJ, Wang MY, Zhu MZ, Xiong WC, Qin XH, Zhu XH (2020) 14,15-epoxyeicosatrienoic acid alleviates pathology in a mouse model of Alzheimer's disease. J Neurosci 40:8188–8203.

Clardy SL, Wang X, Zhao W, Liu W, Chase GA, Beard JL, Felt BT, Connor JR (2006) Acute and chronic effects of developmental iron deficiency on mRNA expression patterns in the brain. J Neural Transm Suppl (71):173–196.

de Andraca I, Castillo M, Walter T (1997) Psychomotor development and behavior in iron-deficient anemic infants. Nutr Rev 55:125–132.

De Pace R, Skirzewski M, Damme M, Mattera R, Mercurio J, Foster AM, Cuitino L, Jarnik M, Hoffmann V, Morris HD, Han TU, Mancini GMS, Buonanno A, Bonifacino JS (2018) Altered distribution of ATG9A and accumulation of axonal aggregates in neurons from a mouse model of AP-4 deficiency syndrome. PLoS Genet 14:e1007363.

Domise M, Sauvé F, Didier S, Caillerez R, Bégard S, Carrier S, Colin M, Marinangeli C, Buée L, Vingtdeux V (2019) Neuronal AMP-activated protein kinase hyper-activation induces synaptic loss by an autophagy-mediated process. Cell Death Dis 10:221.

Duce JA, et al. (2010) Iron-export ferroxidase activity of β-amyloid precursor protein is inhibited by zinc in Alzheimer's disease. Cell 142:857–867.

Estebanez L, Hoffmann D, Voigt BC, Poulet JFA (2017) Parvalbumin-expressing GABAergic neurons in primary motor cortex signal reaching. Cell Rep 20:308–318.

Fink JK (2013) Hereditary spastic paraplegia: clinico-pathologic features and emerging molecular mechanisms. Acta Neuropathol 126:307–328.

Friedman A, et al. (2020) Striosomes mediate value-based learning vulnerable in age and a Huntington's disease model. Cell 183:918–934.e49.

Gritton HJ, Howe WM, Romano MF, DiFeliceantonio AG, Kramer MA, Saligrama V, Bucklin ME, Zemel D, Han X (2019) Unique contributions of parvalbumin and cholinergic interneurons in organizing striatal networks during movement. Nat Neurosci 22:586–597.

Heizmann CW, Berchtold MW, Rowlerson AM (1982) Correlation of parvalbumin concentration with relaxation speed in mammalian muscles. Proc Natl Acad Sci U S A 79:7243–7247.

Hou YH, Luan JY, Huang TD, Deng TC, Li X, Xiao ZF, Zhan JH, Luo D, Hou Y, Xu LL, Lin DK (2021) Tauroursodeoxycholic acid alleviates secondary injury in spinal cord injury mice by reducing oxidative stress, apoptosis, and inflammatory response. J Neuroinflammation 18:216.

Johnstone D, Milward EA (2010) Genome-wide microarray analysis of brain gene expression in mice on a short-term high iron diet. Neurochem Int 56:856–863.

Kern H, Hofer C, Mödlin M, Mayr W, Vindigni V, Zampieri S, Boncompagni S, Protasi F, Carraro U (2008) Stable muscle atrophy in long-term paraplegics with complete upper motor neuron lesion from 3- to 20-year SCI. Spinal Cord 46:293–304.

Klebe S, et al. (2012) KIF1A missense mutations in SPG30, an autosomal recessive spastic paraplegia: distinct phenotypes according to the nature of the mutations. Eur J Hum Genet 20:645–649.

Legay C, Mei L (2017) Moving forward with the neuromuscular junction. J Neurochem 142:59–63.

Levy JE, Jin O, Fujiwara Y, Kuo F, Andrews NC (1999) Transferrin receptor is necessary for development of erythrocytes and the nervous system. Nat Genet 21:396–399.

Lin YT, Chen JC (2018) Dorsal root ganglia isolation and primary culture to study neurotransmitter release. J Vis Exp (140):57569.

Liu K, Lei R, Li Q, Wang XX, Wu Q, An P, Zhang JC, Zhu MY, Xu ZH, Hong Y, Wang FD, Shen Y, Li HC, Li HS (2016) Transferrin receptor controls AMPA receptor trafficking efficiency and synaptic plasticity. Sci Rep 6:21019.

Ljungberg L, Lang-Ouellette D, Yang A, Jayabal S, Quilez S, Watt AJ (2016) Transient developmental Purkinje cell axonal torpedoes in healthy and ataxic mouse cerebellum. Front Cell Neurosci 10:248.

Matak P, Matak A, Moustafa S, Aryal DK, Benner EJ, Wetsel W, A NC (2016) Disrupted iron homeostasis causes dopaminergic neurodegeneration in mice. Proc Natl Acad Sci U S A 113:3428–3435.

Misgeld T, Schwarz TL (2017) Mitostasis in neurons: maintaining mitochondria in an extended cellular architecture. Neuron 96:651–666.

Möller HE, Bossoni L, Connor JR, Crichton RR, Does MD, Ward RJ, Zecca L, Zucca FA, Ronen I (2019) Iron, myelin, and the brain: neuroimaging meets neurobiology. Trends Neurosci 42:384–401.

Montenegro G, et al. (2012) Mutations in the ER-shaping protein reticulon 2 cause the axon-degenerative disorder hereditary spastic paraplegia type 12. J Clin Invest 122:538–544.

Muckenthaler MU, Rivella S, Hentze MW, Galy B (2017) A red carpet for iron metabolism. Cell 168:344–361.

Nuber S, Rajsombath M, Minakaki G, Winkler J, Müller CP, Ericsson M, Caldarone B, Dettmer U, Selkoe DJ (2018) Abrogating native α-synuclein tetramers in mice causes a L-DOPA-responsive motor syndrome closely resembling Parkinson's disease. Neuron 100:75–90.e5.

Oates EC, et al. (2013) Mutations in BICD2 cause dominant congenital spinal muscular atrophy and hereditary spastic paraplegia. Am J Hum Genet 92:965–973.

Osseward PJ, Pfaff SL (2019) Cell type and circuit modules in the spinal cord. Curr Opin Neurobiol 56:175–184.

Paldino E, D'angelo V, Massaro Cenere M, Guatteo E, Barattucci S, Migliorato G, Berretta N, Riess O, Sancesario G, Mercuri NB, Fusco FR (2022) Neuropathology of the basal ganglia in SNCA transgenic rat model of Parkinson's disease: involvement of parvalbuminergic interneurons and glial-derived neurotropic factor. Int J Mol Sci 23:10126.

Pamukcu A, Cui Q, Xenias HS, Berceau BL, Augustine EC, Fan I, Chalasani S, Hantman AW, Lerner TN, Boca SM, Chan CS (2020) Parvalbumin+ and Npas1+ pallidal neurons have distinct circuit topology and function. J Neurosci 40:7855–7876.

Qiang L, Piermarini E, Muralidharan H, Yu W, Leo L, Hennessy LE, Fernandes S, Connors T, Yates PL, Swift M, Zholudeva LV, Lane MA, Morfini G, Alexander GM, Heiman-Patterson TD, Baas PW (2019) Hereditary spastic paraplegia: gain-of-function mechanisms revealed by new transgenic mouse. Hum Mol Genet 28:1136–1152.

Rouault TA (2013) Iron metabolism in the CNS: implications for neurodegenerative diseases. Nat Rev Neurosci 14:551–564.

Sahni V, Shnider SJ, Jabaudon D, Song JHT, Itoh Y, Greig LC, Macklis JD (2021) Corticospinal neuron subpopulation-specific developmental genes prospectively indicate mature segmentally specific axon projection targeting. Cell Rep 37:109843.

Salinas S, Proukakis C, Crosby A, Warner TT (2008) Hereditary spastic paraplegia clinical features and pathogenetic mechanisms. Lancet Neurol 7:1127–1138.

Santiago González DA, Cheli VT, Wan R, Paez PM (2019) Iron metabolism in the peripheral nervous system: the role of DMT1, ferritin, and transferrin receptor in Schwann cell maturation and myelination. J Neurosci 39:9940–9953.

Schüle R, et al. (2016) Hereditary spastic paraplegia: clinicogenetic lessons from 608 patients. Ann Neurol 79:646–658.

Schuurs-Hoeijmakers JH, et al. (2012) Mutations in DDHD2, encoding an intracellular phospholipase A_1, cause a recessive form of complex hereditary spastic paraplegia. Am J Hum Genet 91:1073–1081.

Senyilmaz D, Virtue S, Xu X, Tan CY, Griffin JL, Miller AK, Vidal-Puig A, Teleman AA (2015) Regulation of mitochondrial morphology and function by stearoylation of TFR1. Nature 525:124–128.

Shafir T, Angulo-Barroso R, Jing YZ, Angelilli ML, Jacobson SW, Lozoff B (2008) Iron deficiency and infant motor development. Early Hum Dev 84:479–485.

Shafir T, Angulo-Barroso R, Su J, Jacobson SW, Lozoff B (2009) Iron deficiency anemia in infancy and reach and grasp development. Infant Behav Dev 32:366–375.

Shribman S, Reid E, Crosby AH, Houlden H, Warner TT (2019) Hereditary spastic paraplegia: from diagnosis to emerging therapeutic approaches. Lancet Neurol 18:1136–1146.

Simpson MA, Cross H, Proukakis C, Pryde A, Hershberger R, Chatonnet A, Patton MA, Crosby AH (2003) Maspardin is mutated in mast syndrome, a complicated form of hereditary spastic paraplegia associated with dementia. Am J Hum Genet 73:1147–1156.

Sohn YS, Breuer W, Munnich A, Cabantchik ZI (2008) Redistribution of accumulated cell iron: a modality of chelation with therapeutic implications. Blood 111:1690–1699.

Tseng PT, Cheng YS, Yen CF, Chen YW, Stubbs B, Whiteley P, Carvalho AF, Li DJ, Chen TY, Yang WC, Tang CH, Chu CS, Yang WC, Liang HY, Wu CK, Lin PY (2018) Peripheral iron levels in children with attention-deficit hyperactivity disorder: a systematic review and meta-analysis. Sci Rep 8:788.

Ueno M, Nakamura Y, Li J, Gu Z, Niehaus J, Maezawa M, Crone SA, Goulding M, Baccei ML, Yoshida Y (2018) Corticospinal circuits from the sensory and motor cortices differentially regulate skilled movements through distinct spinal interneurons. Cell Rep 23:1286–1300.e7.

Verret L, Mann EO, Hang GB, Barth AM, Cobos I, Ho K, Devidze N, Masliah E, Kreitzer AC, Mody I, Mucke L, Palop JJ (2012) Inhibitory interneuron deficit links altered network activity and cognitive dysfunction in Alzheimer model. Cell 149:708–721.

Wang Z, Zeng YN, Yang P, Jin LQ, Xiong WC, Zhu MZ, Zhang JZ, He X, Zhu XH (2019) Axonal iron transport in the brain modulates anxiety-related behaviors. Nat Chem Biol 15:1214–1222.

Wang ZZ, Yin WJ, Zhu LZ, Li J, Yao YK, Chen FF, Sun MM, Zhang JY, Shen N, Song Y, Chang X (2018) Iron drives T helper cell pathogenicity by promoting RNA-binding protein PCBP1-mediated proinflammatory cytokine production. Immunity 49:80–92.e7.

Ward RJ, Zucca FA, Duyn JH, Crichton RR, Zecca L (2014) The role of iron in brain ageing and neurodegenerative disorders. Lancet Neurol 13:1045–1060.

Wertman V, Gromova A, Spada ARL, Cortes CJ (2019) Low-cost gait analysis for behavioral phenotyping of mouse models of neuromuscular disease. J Vis Exp (149):10.3791/59878.

Woodin MA, Kim JC, Robertson J, Zinman L, Keith J, De Koninck Y, Côté D, Gasecka A, Keramidis I, Garand D, Yang JW, Bedard S, Pressey JC, Liang X, Dargaei Z, Place KM, Aqrabawi AJ, Khademullah CS (2020) Cortical interneuron-mediated inhibition delays the onset of amyotrophic lateral sclerosis. Brain 143:800–810.

Wu HT, Li Y, Cheng JX, Yang HH, Chen LP, Liu FJ, Wu Y, Fan M (2021) Transferrin receptor 1 plays an important role in muscle development and denervation-induced muscular atrophy. Neural Regen Res 16:1308–1316.

Xu W, Barrientos T, Mao L, Rockman HA, Sauve AA, Andrews NC (2015) Lethal cardiomyopathy in mice lacking transferrin receptor in the heart. Cell Rep 13:533–545.

Yang XF, Xue PP, Yuan M, Xu X, Wang C, Li WQ, Machens HG, Chen ZB (2021) SESN2 protects against denervated muscle atrophy through unfolded protein response and mitophagy. Cell Death Dis 12:805.

Ying YB, Huang ZY, Tu YR, Wu QJ, Li ZY, Zhang YF, Yu HL, Zeng AN, Huang HZ, Ye JH, Ying WY, Chen M, Feng ZY, Xiang ZY, Ye QS, Zhu SP, Wang ZG (2023) A shear-thinning, ROS-scavenging hydrogel combined with dental pulp stem cells promotes spinal cord repair by inhibiting ferroptosis. Bioact Mater 22:274–290.

Zhang J, Weinrich JAP, Russ JB, Comer JD, Bommareddy PK, DiCasoli RJ, Wright CVE, Li Y, van Roessel PJ, Kaltschmidt JA (2017) A role for dystonia-associated genes in spinal GABAergic interneuron circuitry. Cell Rep 21:666–678.

Zhou JH, Wang XT, Zhou L, Zhou L, Xu FX, Su LD, Wang H, Jia F, Xu FQ, Chen GQ, De Zeeuw CI, Shen Y (2017) Ablation of TFR1 in Purkinje cells Inhibits mGlu1 trafficking and impairs motor coordination, but not autistic-like behaviors. J Neurosci 37:11335–11352.